

A Universal Scaling Law for Mitotic Spindles Driven by Chromosome Crowding

Lovro Gudlin^{1,2,*}, Kruno Vukušić^{1,*}, Maja Novak^{3,*}, Monika Trupinić¹, Matko Ljulj⁴, Iva Dundović¹, Ana Petelinec¹, Loren Petrušić¹, Anna Hertel⁵, Thomas van Ravesteyn⁶, Marianna Trakala⁷, Geert J. P. L. Kops⁶, Zuzana Storchová⁵, Josip Tambača⁴, Nenad Pavin^{3,#}, Iva M. Tolić^{1,#}

¹Division of Molecular Biology, Ruđer Bošković Institute, Zagreb, Croatia.

²Doctoral study of Biophysics, Faculty of Science, University of Split, Split, Croatia.

³Department of Physics, University of Zagreb, Zagreb, Croatia.

⁴Department of Mathematics, University of Zagreb, Zagreb, Croatia.

⁵Department of Molecular Genetics, RPTU Kaiserslautern-Landau, Kaiserslautern, Germany.

⁶Oncode Institute, Hubrecht Institute, Royal Netherlands Academy of Arts and Sciences (KNAW), University Medical Center Utrecht, Utrecht, the Netherlands.

⁷Koch Institute for Integrative Cancer Research, Massachusetts Institute of Technology, Cambridge, Massachusetts, USA.

*These authors contributed equally to this work.

#Corresponding authors: npavin@phy.hr, tolic@irb.hr

Abstract

Cells regulate the size of their internal structures to maintain function in diverse biological settings¹. The mitotic spindle, a molecular micro-machine responsible for chromosome segregation², must scale to accommodate genomes varying in size by over 10,000-fold across eukaryotes³. Yet, how spindle biomechanics adapts to vastly different genome sizes remains unknown. Here, we uncover a universal spindle scaling law, where metaphase plate width scales with genome size following a power law with an exponent of $\sim 1/3$. We hypothesize that chromosome crowding within the metaphase plate generates compressive forces as chromosomes push against each other, thereby determining spindle size and shape. Our experiments with altered chromosome number and mechanical properties in healthy and cancerous human and mouse cells, together with a theoretical model based on inter-chromosome pushing forces and mechanical manipulations of cells, confirm this hypothesis. Extending these insights across eukaryotes, we demonstrate that chromosome crowding predicts the observed power-law scaling. The biophysical constraint of chromosome crowding offers a mechanistic explanation for the evolution of open mitosis and mitotic cell rounding, enabling the division of larger genomes. Spindle adaptability to larger genomes may promote the proliferation of polyploid cells, driving not only tumor progression but also speciation during evolution.

Size control is a universal regulatory principle in biology, ensuring that cellular structures scale precisely to maintain function and adaptability¹. This challenge is particularly evident in mitosis, where the mitotic spindle must be properly scaled to divide the chromosomes accurately. Failure in this process can lead to aneuploidy, a key feature of cancer and developmental disorders⁴.

Across all eukaryotes, spindles are composed of microtubules, motor proteins, and kinetochores, which link chromosomes to spindle fibers and align them at the metaphase plate². Despite their conserved molecular components, spindles have evolved diverse morphologies to adapt to different biological conditions, with pole organization varying from centrosome-focused to unfocused, kinetochore structure from monocentric to holocentric, and the mode of mitosis from closed to open⁵. In particular, spindle size is adapted to large variations in cell size during embryonic development within individual species and to different genome sizes across species⁶. As cells shrink during early embryonic development, spindle size decreases accordingly, regulated by mechanisms that control microtubule nucleation and dynamics in a cell size-dependent manner⁶⁻¹⁷.

In contrast to cell size, spindle adaptation to genome size across species has been more challenging to study due to vast and multilayered biological diversity among different organisms. Previous studies found that the genome size affects spindle geometry within a single or a few related species¹⁸⁻²¹, while others reported no effect²². Looking more broadly across all eukaryotes, it is remarkable that spindles vary in size about 100-fold, from less than 1 to 60 μm , together with the genome sizes variation of more than 10,000-fold^{3,8,23}. Considering the extensive diversity in spindle sizes and shapes across eukaryotes, it remains uncertain whether a universal principle exists to explain how spindles handle genomes of such wide-ranging sizes.

Spindle scaling across eukaryotes and cell ploidies

A potential evolutionarily conserved principle of spindle adaptation may be identified from the relationship between spindle and genome sizes across eukaryotes. To explore this relationship, we used published measurements or measured in published images the length and width of the spindle, as well as the width of the metaphase plate in 25 eukaryotic species from diverse lineages (Fig. 1a, b, Extended Data Fig. 1a and Table 1). For multicellular organisms with cells of varying sizes, we analyzed only differentiated cells, as they are smaller and provide less space for the same set of chromosomes than larger embryonic cells. This approach allows us to assess the lower physical limit of spindle size. Our analysis revealed that the metaphase plate width shows a sublinear relationship with the genome size (Fig. 1c). As the genome size covers 4 orders of magnitude, we plot the data on a log-log scale. Here the data align at a straight line, revealing a power-law scaling of the metaphase plate width with the genome size, with a scaling exponent of 0.33 and a significant correlation ($R^2 = 0.95$, $p = 10^{-16}$) (Fig. 1d). These results suggest the existence of a conserved mechanism of spindle adaptation to genome size from yeasts to animals and plants.

Spindle length and width also follow a power law (Fig. 1e, and Extended Data Fig. 1b). However, their correlation with genome size is weaker compared to that of metaphase plate width (z-score = 3.52, $p = 0.0002$, and z-score = 2.41, $p = 0.008$ for spindle length and width, respectively), suggesting that spindle and metaphase plate dimensions are regulated by

different mechanisms. In contrast to the correlation with the genome size, metaphase plate and spindle dimensions were not correlated with the number of chromosomes ($R^2 = 0.06$, $p = 0.26$, Fig. 1f, and Extended Data Fig. 1c, d). We infer that the total amount of chromatin in the metaphase plate, rather than the chromosome number and the spindle length, is at the core of the spindle adaptation mechanism.

To uncover the physics behind the identified scaling law, we start by exploring the interplay between the mechanics of the mitotic spindle and chromosomes, which are aligned at the metaphase plate by microtubules and motor proteins^{24,25}. We hypothesize that crowding of chromosomes, as they “fight for space” within the metaphase plate, results in inter-chromosome pushing forces which increase the plate and spindle width. This hypothesis is supported by the tight packing of chromosomes within the metaphase plate²⁶, where they repulse each other by steric forces arising from chromosome compaction and by electrostatic interactions^{27–30}. Alternatively, spindle geometry may be set by self-organization of the microtubule network^{22,31}. Here, we provide four lines of evidence in support of the chromosome crowding hypothesis, where we probed human and mouse mitotic spindles by altering the amount and the mechanical properties of chromatin.

First, we increased the cell ploidy. We used hypo-tetraploid clones derived from human healthy and tumor cell lines, which have undergone long-term adaptation after cytokinesis failure and divide in a bipolar manner^{32,33} (Fig. 2a, and Extended Data Fig. 2a, b). To generate newly-formed tetraploid and hypooctaploid cells with bipolar spindles, we designed a novel strategy (Extended Data Fig. 2c) by preventing centriole overduplication³⁴ after induced polyploidization through mitotic slippage³⁵, to avoid formation of multipolar spindles³⁶. We found that metaphase plate width and thickness, as well as spindle length and width, increased with ploidy, regardless of the cell type and the polyploidy-generation method (Fig. 2b, Extended Data Fig. 2d-f, Fig. 3a-c, and Movie 1). The spindle widening following polyploidization was not dependent on the presence of centrioles at the spindle poles (Extended Data Fig. 4a-c). To test the relationship between the plate width and chromosome number on a cell-by-cell basis, we used the nuclear area in prophase as a proxy for the chromosome number in each cell³⁵ (Extended Data Fig. 4d, and Movie 1). The metaphase plate width correlated with the nuclear area and a power-law fit yielded an exponent of 0.29 (Fig. 2c), matching the scaling found across eukaryotes. Increased ploidy affects not only chromosome and centrosome numbers, but also the transcriptome^{37,38}. Indeed, our transcriptome analysis showed upregulation of key spindle assembly and kinesin family genes (e.g., *AURKB*, *AURKA*, *KIF4A*) in adapted tetraploid cells (Extended Data Fig. 5a-c), suggesting adaptive mechanisms to adjust spindle length in response to increased spindle width from higher chromosome numbers.

Second, we took advantage of natural variation in ploidy in patient-derived colorectal cancer organoids³⁹ (Fig. 2d). We found correlation between metaphase plate width and nuclear area with a similar power-law scaling (Fig. 2e), whereas metaphase plate thickness exhibited only a weak linear correlation with nuclear area (Extended Data Fig. 3c), as in the healthy human cell line and its derivatives of various ploidy (Fig. 2c, Extended Data Fig. 3a). In agreement with these results, naturally occurring polyploids among healthy primary mouse

small intestinal cells grown in 3D⁴⁰ had wider metaphase plates, as well as wider and longer spindles (Fig. 2f, g, and Extended Data Fig. 4e).

Third, we reduced the number of chromosomes in the metaphase plate by depleting CENP-E/kinesin-7 in otherwise healthy diploid cells, resulting in hypodiploid metaphase plates with a few chromosomes at the spindle poles, which could be precisely quantified in individual cells (Extended Data Fig. 4f). Within a population of CENP-E-depleted cells, those with fewer chromosomes in the metaphase plate displayed progressively thinner spindles (Extended Data Fig. 4f, g). Similarly, metaphase plates in published images of near-haploid human tumor cells⁴¹ were 18% narrower than their near-diploid counterparts (Extended Data Table 2).

Fourth, we reduced chromatin content in the metaphase plate and disrupted chromosome structure by inducing mitosis with an unreplicated genome (MUG)⁴² in a tumor cell line (Fig. 2h). In MUG cells, where centromeres are aligned on the spindle but most of the uncondensed chromatin is displaced in the cytoplasm, spindles were 43% thinner while maintaining their length (Fig. 2i; note that the metaphase plate width cannot be determined due to uncondensed chromatin). Taken together, these experiments indicate that the amount of chromatin and its mechanical properties determine spindle width.

To investigate whether the observed spindle scaling is conserved in naturally acentriolar cells, we analyzed published images of mammalian meiotic and early embryonic spindles. Consistent with the chromosome crowding hypothesis, metaphase I plates—having twice the ploidy of metaphase II plates—were 23% wider in human oocytes and 33% wider in mouse oocytes in comparison with metaphase II plates (Extended Data Table 2)^{43–48}. Despite the variation in plate width, length differed by no more than 7% between metaphase I and II spindles (Extended Data Table 2). Similarly, tetraploidization increased the width of the metaphase plate by 17% in mouse early embryonic cells and 26% in porcine oocytes, while having a significantly smaller impact on spindle length (Extended Data Fig. 4h and Table 2) or metaphase plate thickness^{49,50}. Collectively, our findings demonstrate that changes in ploidy are accompanied by corresponding changes in spindle width across different systems, while spindle length does not necessarily change with ploidy. This supports the hypothesis that chromosome crowding sets spindle width in mitosis and meiosis across diverse culturing conditions, cell types, and species.

Inter-chromosome pushing forces set spindle size

To design direct biomechanical tests of the chromosome crowding hypothesis, with the ultimate aim of explaining the spindle scaling law, we introduced a physical model of the metaphase plate. As this hypothesis remains untested, we designed a minimal model where spindle shape is determined by chromosomes and microtubules, while omitting proteins unrelated to the hypothesis, such as microtubule-associated proteins (MAPs). We assume that chromosomes, represented as elastic objects⁵¹ at the spindle midplane, push on their neighbors by elastic forces (Fig. 3a, and Box 1). We use spheres as the simplest geometric representation of chromosome shape, taking their volume as a proxy for DNA content. The inter-chromosome pushing forces bend the attached microtubules, which in turn compress the spheres, setting the width of the metaphase plate and of the spindle (Box 1, Methods). Thus, the metaphase plate width is a readout of the force by which the neighboring spheres push each other.

We start exploring the spindle biomechanics in the model by asking how chromosome properties affect spindle shape and the underlying inter-chromosome pushing forces. Our numerical calculations produce a typical shape of the spindle and predict only slight deformation of spheres (Fig. 3a), for the known elasticity of chromatin and microtubules^{52,53}. As expected for small deformation of spheres, the model predicts a power-law scaling of the metaphase plate width with the sphere volume, with a scaling exponent of 0.37 (Fig. 3b). This exponent can be intuitively understood as the relationship between a linear scale of an object and its volume, which scales with an exponent of 1/3. Similarly, the model predicts a power-law scaling of the metaphase plate width with the number of spheres, but with a larger exponent of 0.43 (Fig. 3c), as expected because the linear dimension of the plate scales with an exponent of 1/2 with its area, which in turn is roughly proportional to the number of spheres. As the number of spheres increases, inter-chromosome pushing forces also increase (Fig. 3d). The outermost sphere experiences the least force because it lacks an external neighbor to exert pressure from the outside. As we move toward the center, each sphere encounters progressively greater forces due to the increasing push exerted by its outer neighbor (Fig. 3a, d).

We compared the model's predictions with the experiments on altered ploidy. For a double chromosome number, the model predicts a 35% wider metaphase plate, obtained by using the scaling from Fig. 3c as $2^{0.43}$. This increase is similar to the one observed in oocytes and early embryonic cells (Extended Data Table 2). By using the same scaling, an increase in the number of chromosomes from 46 to 77 gives a 25% wider plate, providing an explanation for the 18-27% wider plates (Extended Data Fig. 2d, e) that we observed in four hypo-tetraploid cell lines with 75-80 chromosomes³². Moreover, the model predicts narrower spindles for smaller or softer spheres, which can explain spindle size in MUG experiments (white line in Fig. 3e). These agreements support our model, prompting us to further challenge its core assumptions.

As the model relies on chromosome and microtubule mechanics, its key test involves acutely perturbing mechanical forces in the spindle, such as applying external compression, rather than altering spindle proteins given their multiple roles in mitosis⁵⁴. The main prediction of the model is that applying compressive force from the top causes an increase in inter-chromosome pushing forces and widening of the metaphase plate, accompanied by a reduction of height and changes of microtubule angles (Fig. 4a-d, and Extended Data Fig. 6a, b). A significant deformation of the metaphase plate occurs as the spheres redistribute under force, with those in the central region undergoing substantial deformation (Fig. 4a). Spindles with smaller or softer spheres also become deformed under compression, but to a smaller extent (Fig. 4c, Extended Data Fig. 6a, b).

To test the model, we acutely squeezed human healthy and tumor cells in metaphase by compressing them with a gel⁵⁵ (Fig. 4e, f). If the chromosomes indeed push each other as in the model, the metaphase plate is expected to widen, even though different outcomes are possible as there are materials that do not widen under pressure, such as cork, or even become narrower⁵⁶. We found that after 1 minute of compression, spindle height in tumor cells decreased by ~44%, the metaphase plate widened by ~30% and thickened by ~50%, while spindle length remained unchanged (Fig. 4g, Extended Data Fig. 6c-e, and Movie 2). Similar trends were observed in healthy cells (Extended Data Fig. 6c-g). Acute compression also

resulted in a wider angle between the outermost microtubule bundles at the spindle pole (Fig. 4h, Extended Data Fig. 6h). When compression was relieved, the metaphase plate partially regained its original width in both cell types (Extended Data Fig. 6c), similar to spindles in previous studies^{55,57}. Spindles in MUG cells also widened upon compression, but only by ~23% (Fig. 4e, g, and Extended Data Movie 2). Both experiments agree with the model's predictions that the spindle widens under compression (compare Fig. 4c, d with Fig. 4g, h). For a quantitative comparison, we identified a compression coefficient of 100 pN/ μm , where the decrease in spindle height predicted by the model is similar to that observed in experiments. The model suggests that the inter-chromosome pushing forces increased 3-fold in the compression experiments (Fig. 4b). As in experiments, the model predicts a larger spindle widening for the parameters corresponding to control than to MUG cells, 39% and 34%, respectively (Fig. 4a, c). Thus, the biomechanical tests inspired and interpreted by the model confirmed the chromosome crowding hypothesis.

Altered metaphase plate shape caused by acute compression might affect mitotic efficiency. Indeed, metaphase was substantially longer in acutely compressed than in uncompressed healthy diploid cells, lasting more than 20 minutes (Extended Data Fig. 6i), compared to less than 10 minutes⁵⁸, respectively. Yet, the majority of compressed cells eventually progressed to anaphase (Extended Data Fig. 6i). Based on these results, we conclude that substantially larger inter-chromosome pushing forces impede mitosis.

Building on our results that spindle width is determined by inter-chromosome pushing forces, and previous findings that spindle length is regulated by MAPs and centrosomes^{16,59}, we asked to what extent these two dimensions are interdependent. After demonstrating their independence in compression experiments, where spindle width increased without a change in length (Extended Data Fig. 6j), we next explored the effects of altering spindle length. In the model, large changes in spindle length result in a mild increase in the spindle width, e.g., when length increases 100%, from 8 to 16 μm , the width increases only about 30% (Fig. 4i, and Extended Data Fig. 6k). This prediction was experimentally validated by perturbing dozens of mitotic MAPs that regulate microtubule dynamics, sliding, and cross-linking in healthy diploid cells⁶⁰, as well as by analyzing polyploid cells with varying numbers of centrosomes. MAP perturbations showed that a 100% increase in spindle length resulted in only a 21% increase in width (Fig. 4j), consistent with model predictions (Fig. 4i). Similarly, spindle length varied with the number of centrosomes at a given ploidy, whereas spindle width exhibited only mild changes (Extended Data Fig. 4b, c). Interestingly, mitotic MAPs were dysregulated in adapted tetraploid cells (Extended Data Fig. 5d), suggesting that these alterations contributed to changes in spindle length in these cells. Altogether, spindle length and width are largely independent, indicating that they are indeed regulated by different mechanisms based on regulation of microtubule dynamics and inter-chromosome pushing forces, respectively (Fig. 4k).

Universality of the chromosome crowding mechanism

As the ultimate aim of our study, we asked whether the proposed mechanism based on inter-chromosome pushing forces is universal and thus can explain the spindle scaling law found across eukaryotes (Fig. 1). To describe different species, we use the model for human spindles

and vary only genome size by modifying chromosome volume, to cover almost 4 orders of magnitude (Box 1). We assume that the volume of a chromosome is proportional to its number of base pairs, as observed for chromosome volume across vertebrate and flowering plant species⁶¹, and in agreement with a comparison of human and yeast chromosomes⁶² (Methods). Thus, chromosomes of all species are represented in the model by spheres with a radius proportional to the 3rd root of genome size (Box 1). Starting from the experimental data point for human spindles, we calculate the metaphase plate width for both smaller and larger genome sizes, thereby extrapolating the model to regions far beyond its original scope. Remarkably, the model predicts a power-law scaling of the metaphase plate width with the genome size, with an exponent of 0.37, close to 0.33 from experiments (Fig. 1d, compare dashed and solid lines), demonstrating the universality of the chromosome crowding hypothesis across very different eukaryotic species.

Discussion

In this work, we identified a conserved mechanism of mitotic spindle adaptation to greatly varying genome sizes from yeasts to plants and animals (Fig. 5). The mechanism is based on metaphase plate and spindle widening driven by inter-chromosome pushing forces. The identified scaling takes into account that chromosome volume is proportional to its genome content (Fig. 1), which was observed across vertebrates and plants⁶¹ as well as for individual human chromosomes⁶³. We propose a broader principle where the degree of chromatin compaction into mitotic chromosomes is conserved across diverse evolutionary lineages, even though genome sizes differ by up to four orders of magnitude. The uniform DNA density of metaphase chromosomes across eukaryotes is likely linked to conserved packing machinery, including histones, cohesins, condensins, and topoisomerases^{64–66}. However, how this machinery produces mitotic chromosomes of similar density and uniform arm length-to-width ratios across eukaryotes, despite vast genome size variation, remains an exciting topic for future studies.

We propose that the magnitude of inter-chromosome forces is influenced not only by chromosome density but also by external forces acting on a cell. This conclusion is supported by our experiments where acute external compression deformed both the cell and spindle, for which the model predicts an increase in inter-chromosome pushing forces from 100 pN to 300 pN (Fig. 4b). The force under compression becomes comparable to the tension force at the kinetochore^{67–69}, which may explain prolonged metaphase in our experiments. Previous studies have shown that cells entering mitosis under confinement form disorganized spindles with high rates of mitotic errors^{70–72}. Our results suggest that errors under confinement arise from chromosome crowding and the excessive inter-chromosome pushing forces, which the spindle microtubules are unable to counteract. The chromosome crowding hypothesis thus explains why cell rounding is a hallmark of eukaryotic cells without a rigid cell wall⁷³ and why eukaryotes with larger genomes undergo open mitosis without a nuclear envelope⁷⁴, as both adaptations create more space for the spindle and chromosomes.

What enables the spindle to reshape itself when faced with an acute increase in inter-chromosome pushing forces? Upon external compression, the angle between microtubules at the spindle pole increases (Fig. 4d, h), suggesting that the microtubules pivot around the pole^{75–}

⁷⁷. We propose that this process facilitates spindle adaptation in cells with centrosomes. Conversely, in spindles with unfocused poles, such as those in plant cells, microtubules appear straight, indicating smaller compression forces. Due to the weaker forces, we speculate that spindles with unfocused poles can more readily accommodate higher ploidy, facilitating polyploidization as an evolutionary advantage for plants in generating new species.

Chromosome crowding leads to spindle scaling with the chromosome number (Figs. 2 and 3c), which explains wider spindles in cells with higher ploidy not only in somatic cells, but also in mammalian oocytes and early embryos. However, during embryogenesis the spindles become narrower even though the number of chromosomes is constant^{17,18,78}, likely due to reduction of chromosome size caused by increased chromosome condensation^{17,79}. Taking into account that excessive inter-chromosome pushing forces arise under confinement, we propose that increased chromosome condensation is important to control these forces and thereby spindle shape, promoting success of early embryogenesis^{80,81}.

Our work reveals that different dimensions of spindle geometry are regulated by distinct mechanisms. Whereas spindle width is determined mainly by chromosome volume, spindle length is controlled by MAPs and influenced by centrosomes in human cells (Figs. 2 and 4j). We propose that these two spindle dimensions are largely independent. This reasoning is in agreement with previous findings that polyploidization in yeast increases spindle width without altering length⁸², and acute microtubule depolymerization in *Xenopus* egg extracts shortens spindles without changing their width⁸³. The independent regulation of spindle length and width may promote spindle adaptation to diverse biological contexts by modifying its shape while preserving functionality. The adaptability of spindle shape is a prerequisite for the proliferation of tetraploid cells, such as those naturally occurring in the human liver⁸⁴. Similarly, it could facilitate the growth of diseased cells, including cancer cells that have undergone tetraploidization or become highly aneuploid due to prior chromosomal missegregation⁸⁵.

Taking a broader perspective across all eukaryotes, we propose that the conserved packing of mitotic chromosomes requires a rather small variation in spindle size for significant changes in genome size. These features together allow the spindle to be built upon the same biological principles across eukaryotes, helping cell diversification without a need for new cell division mechanisms. We suggest that the spindle's biomechanical adaptability promotes evolution by allowing the division of substantially altered genomes after speciation-driving events such as polyploidization⁸⁶.

Methods

The model for mitotic spindle based on the inter-chromosome pushing forces

Geometry. In our three-dimensional model, mitotic spindle has length L and it is composed of N microtubule bundles that extend between two spindle poles, where the geometry is parametrized by Cartesian coordinates with x -, y - and z -axes, and the associated unit vectors, $\hat{\mathbf{x}}$, $\hat{\mathbf{y}}$, and $\hat{\mathbf{z}}$ (Fig. 3, Extended Data Fig. 7a-d). In our description, the spindle is aligned to the x -axis, with the left and right poles located at points $(0, 0, 0)$ and $(L, 0, 0)$, respectively (Extended Data Fig. 7a). Poles are connected by the radius vector $\mathbf{L} = L\hat{\mathbf{x}}$. A point along the contour of bundle i is denoted by radius vector $\mathbf{r}_i(s)$, which is a function of contour length s (Extended Data Fig. 7d). In order to simplify calculations, we use a small angle approximation, $s \approx x$, which is a plausible approach for the majority of spindle microtubules⁸⁷. A chromosome is bound to microtubule bundle at position $\mathbf{r}_{i,\text{chr}}$, with projection onto x -axis that is equal for all chromosomes, $x_{\text{chr}} = \mathbf{r}_{i,\text{chr}} \cdot \hat{\mathbf{x}}$. In the case of chromosomes aligned within the metaphase plane they obey $x_{\text{chr}} = L/2$ (Extended Data Fig. 7d). Positions of the microtubule bundle ends, $\mathbf{d}_{i,\text{left}} \equiv \mathbf{r}_i(0)$ and $\mathbf{d}_{i,\text{right}} \equiv \mathbf{r}_i(L) - \mathbf{L}$, are defined relative to the left and right poles, respectively.

Mechanical balance. In our theory we consider mitotic spindle as a static object. Thus, we impose a balance of forces and torques for each individual bundle and pole. The balance of forces for the bundle i reads

$$\mathbf{F}_{i,\text{left}} + \mathbf{F}_{i,\text{chr}} + \mathbf{F}_{i,\text{right}} = 0. \quad (\text{M1})$$

Here, vectors $\mathbf{F}_{i,\text{left}}$ and $\mathbf{F}_{i,\text{right}}$ denote forces exerted on the bundle by the left and the right pole, respectively. We also consider force $\mathbf{F}_{i,\text{chr}}$ which is exerted by the chromosome attached to bundle i . This force arises from inter-chromosome pushing forces,

$$\mathbf{F}_{i,\text{chr}} = \sum_{j \neq i}^N \mathbf{F}_{ij}. \quad (\text{M2})$$

Here, vector \mathbf{F}_{ij} denotes the force by which chromosomes j pushes chromosomes i , with the opposing force obeying $\mathbf{F}_{ji} = -\mathbf{F}_{ij}$ (Extended Data Fig. 7c). In Box 1, Eq. (3) offers a simplified version of Eq. (M2), explicitly stating in words that the sum is restricted to contributions from neighboring chromosomes. The torques for the bundle i are also in balance, which for the left bundle end reads

$$\mathbf{M}_{i,\text{left}} + (\mathbf{r}_{i,\text{chr}} - \mathbf{d}_{i,\text{left}}) \times \mathbf{F}_{i,\text{chr}} + (\mathbf{L} - \mathbf{d}_{i,\text{left}} + \mathbf{d}_{i,\text{right}}) \times \mathbf{F}_{i,\text{right}} + \mathbf{M}_{i,\text{right}} = 0. \quad (\text{M3})$$

Here $\mathbf{M}_{i,\text{left}}$ and $\mathbf{M}_{i,\text{right}}$ denote torques exerted by two respective spindle poles on the bundle i . Eqs. (M1)-(M3) together describe the mechanical balance of the individual microtubule bundles.

The model also includes balance for the spindle poles. We first introduce theoretical description for the left pole. Balance of forces and torques for the left pole read:

$$\sum_{i=1}^N \mathbf{F}_{i,\text{left}} = 0 \quad (\text{M4})$$

and

$$\sum_i^N \mathbf{d}_{i,\text{left}} \times \mathbf{F}_{i,\text{left}} + \sum_i^N \mathbf{M}_{i,\text{left}} = 0. \quad (\text{M5})$$

Experiments show that microtubule bundle pivots around the spindle pole under external force⁷⁶, which we include in the model by assuming a freely joint condition $\mathbf{M}_{i,\text{left}} = \mathbf{M}_{i,\text{right}} = 0$. Note that balance at the right pole is described by an analogous set of equations which can be obtained by replacing index ‘left’ with index ‘right’ in Eqs. (M4) and (M5). These equations, together with Eqs. (M1)-(M3), describe the mechanical balance of the entire spindle.

Inter-chromosome pushing forces. A chromosome is modeled as an elastic sphere of radius R with a corresponding volume, $V = \frac{4\pi}{3}R^3$. The genome size is proportional to total volume of all chromosomes, $G = \rho NV$, where ρ denotes the DNA density⁶¹. This relationship is given in Box 1 as Eq. (2). Thus, a direct link between sphere radius and genome size is given by

$$R = \left(\frac{3G}{4\pi N\rho} \right)^{1/3}. \quad (\text{M6})$$

A chromosome deforms under pushing forces exerted by its neighbors. The reduction in the distance between chromosomes, $h_{ij} = (2R - |\mathbf{r}_{i,\text{chr}} - \mathbf{r}_{j,\text{chr}}|)\theta(2R - |\mathbf{r}_{i,\text{chr}} - \mathbf{r}_{j,\text{chr}}|)$ (Extended Data Fig. 7c), reflects the extent of their deformation (Fig. 3a). Here, the Heaviside step function θ ensures that there is no force acting on spheres if they are not in contact. This deformation results with repulsive force, which for small deformations reads⁸⁸

$$\mathbf{F}_{ij} = -ch_{ij}^{3/2} \frac{\mathbf{r}_{i,\text{chr}} - \mathbf{r}_{j,\text{chr}}}{|\mathbf{r}_{i,\text{chr}} - \mathbf{r}_{j,\text{chr}}|}. \quad (\text{M7})$$

A simplified version of Eq. (M7) is given as Eq. (1) in Box 1, where we calculate a magnitude of inter-chromosome pushing force only. The elasticity constant c is calculated assuming that spheres are elastic objects described by Young’s modulus E and Poisson ratio σ ,

$$c = \frac{1}{3} \frac{E}{1 - \sigma^2} \sqrt{2R}. \quad (\text{M8})$$

Shape of flexible microtubule bundle. In order to predict the shape of microtubule bundles, which sets geometry of the spindle, we calculate how microtubules deform under force and torque. We parametrize microtubule bundle shape by the unit tangent vector, $\mathbf{t}_i(s) = d\mathbf{r}_i/ds$ (Extended Data Fig. 7d), and the angle that describes the orientation of the cross-section relative to one of the straight bundle, $\phi_i(s)$. The shape of the slender rod is given by the static Kirchhoff equation,

$$\kappa \mathbf{t}_i \times \frac{d\mathbf{t}_i}{ds} + \tau \frac{d\phi_i}{ds} \mathbf{t}_i = -\mathbf{M}_i. \quad (\text{M9})$$

Here, the parameters κ and τ denote flexural and torsional rigidity, respectively. To calculate the torque in Eq. (M9), we solve the balance of torque on segment of elastic rod,

$$\frac{d\mathbf{M}_i}{ds} = -\mathbf{t}_i \times \mathbf{F}_i, \quad (\text{M10})$$

where \mathbf{F}_i denotes a contact force at position s . To integrate Eq. (M10) we take into account that contact force has a jump at $x = L/2$. In the small angle approximation we obtain $\mathbf{M}_i(x) = \mathbf{M}_i(0) - (\mathbf{r}_i - \mathbf{d}_{i,\text{left}}) \times \mathbf{F}_{i,\text{left}}$ for $x < L/2$ and $\mathbf{M}_i(x) = \mathbf{M}_i(0) - (\mathbf{r}_i - \mathbf{d}_{i,\text{left}}) \times \mathbf{F}_{i,\text{left}} - (\mathbf{r}_i - \mathbf{r}_{i,\text{chr}}) \times \mathbf{F}_{i,\text{chr}}$ for $x > L/2$. After implementing boundary conditions $\mathbf{M}_i(0) = \mathbf{M}_i(L) = 0$ the contact torque along the contour, exerted by the portion of rod from the left microtubule end, is calculated as

$$\mathbf{M}_i(s) = -(\mathbf{r}_i - \mathbf{d}_{i,\text{left}}) \times \mathbf{F}_{i,\text{left}} - (\mathbf{r}_i - \mathbf{r}_{i,\text{chr}}) \times \mathbf{F}_{i,\text{chr}} \theta(x - x_{\text{chr}}). \quad (\text{M11})$$

The Heaviside step function ensures that force $\mathbf{F}_{i,\text{chr}}$ is exerted at the position of chromosome i . We also assume that microtubule bundles have the same force parallel with the main spindle axis and from Eq. (M4) follows that it has a vanishing value, $\hat{\mathbf{x}} \cdot \mathbf{F}_{i,\text{left}} = 0$.

In order to solve the model, we first calculate a microtubule shape by solving Eq. (M9). We solve it in a small angle approximation, together with the other previously stated assumptions, namely (i) chromosomes are positioned within the metaphase plane, (ii) the microtubule-pole connection is freely jointed, and (iii) there is no force parallel with main spindle axis. In the case of a spindle with mirror symmetry, where the metaphase plate is a plane of symmetry, Eqs. (M1) and (M3) yield $\mathbf{F}_{i,\text{left}} = -\frac{1}{2} \mathbf{F}_{i,\text{chr}}$. In this case the corresponding microtubule bundle lies within a plane. In particular, for force exerted by the chromosome pointing in the direction of y axis and magnitude $F_{i,\text{chr}} \equiv |\mathbf{F}_{i,\text{chr}}|$, Eq. (M9) simplifies to $d^2y/dx^2 = -F_{i,\text{chr}}x/(2\kappa)$, for $x < L/2$, which is given as Eq. (4) in Box 1.

Position of microtubule bundle ends. Microtubule bundle ends are located at nodes of the finite two-dimensional hexagonal lattice (Extended Data Fig. 7b). The lattice parameter, a_0 , represents the nearest-neighbor distance between lattice nodes situated within a single plane. We consider the cases where $N = 1 + 3(m + 1)m$ nodes are distributed within the lattice such that comprise a regular hexagon with edge of length a_0m . For this reason, we consider the cases with $N = 7, 19, 37, 61, 91$ microtubule bundles which correspond to $m = 1, 2, 3, 4, 5$, respectively. The center of the lattice corresponds to spindle pole, whereas the lattice plane is perpendicular to \mathbf{x} -axis.

External compressive force. To describe experiments in which spindles are compressed by external forces, we change the Eq. (M2) by adding the force, $\mathbf{F}_{i,\text{ext}}$, that arises from interactions of chromosomes with the external probe,

$$\mathbf{F}_{i,\text{chr}} = \sum_{j \neq i}^N \mathbf{F}_{ij} + \mathbf{F}_{i,\text{ext}}. \quad (\text{M12})$$

Interactions with the external probe are approximated by the linear elastic restoring force, $\mathbf{F}_{i,\text{ext}} = -k(\hat{\mathbf{y}} \cdot \mathbf{r}_{i,\text{chr}})\hat{\mathbf{y}}$, where k denotes a phenomenological compression coefficient. In experiments, external forces influence the spindle poles, ensuring the spindle remains aligned with the cover slip. In our theoretical approach, this is modeled by constraining the spindle pole positions to remain located at points $(0, 0, 0)$ and $(L, 0, 0)$ under compression.

Numerical procedure. For numerical computations of the complete spindle, we reformulate the model as a problem of minimizing the total energy. Under the small-angle approximation, the potential bending energy of the i th bundle, as described by Kirchhoff's equation (M9), is expressed as

$$V_{\text{bend}}(\mathbf{r}_i) = \frac{1}{2} \kappa \int_0^L \left(\frac{d^2 \mathbf{r}_i}{ds^2} \cdot \hat{\mathbf{y}} \right)^2 + \left(\frac{d^2 \mathbf{r}_i}{ds^2} \cdot \hat{\mathbf{z}} \right)^2 dx, \quad (\text{M13})$$

where $\mathbf{r}_i \cdot \hat{\mathbf{y}}$ and $\mathbf{r}_i \cdot \hat{\mathbf{z}}$ describe transversal displacements. For a detailed derivation of these equations from three-dimensional linearized elasticity, refer to⁸⁹. The potential associated with the repulsive force between i th and j th chromosomes, as given in Eq. (M7), is given by

$$V_{\text{chr}}(\mathbf{r}_i, \mathbf{r}_j) = \frac{2}{5} ch_{ij}^{5/2}. \quad (\text{M14})$$

The third potential we consider arises from the linear elastic restoring force at the i th chromosome. This potential is given by

$$V_{\text{ext}}(\mathbf{r}_i) = \frac{1}{2} k (\hat{\mathbf{y}} \cdot \mathbf{r}_{i,\text{chr}})^2. \quad (\text{M15})$$

The total potential of the entire spindle, incorporating the repulsive forces between chromosomes and the restoring forces, can now be expressed as the sum of all potentials from Eqs. (M13), (M14), and (M15) across all bundles with parametrizations collected in $\mathbf{r} = (\mathbf{r}_1, \dots, \mathbf{r}_N)$

$$V(\mathbf{r}) = \sum_{i=1}^N V_{\text{bend}}(\mathbf{r}_i) + \sum_{i,j=1, i < j}^N V_{\text{chr}}(\mathbf{r}_i, \mathbf{r}_j) + \sum_{i=1}^N V_{\text{ext}}(\mathbf{r}_i). \quad (\text{M16})$$

Then the equilibrium configuration \mathbf{r} of the spindle minimizes the functional V over the set of bundle parametrizations that satisfy the specified boundary conditions. To solve this minimization problem, we discretize it using the finite element method as described in⁹⁰ and employ the gradient descent type method as in⁹¹ to approximate the minimizer.

Our model for mitotic spindle is given by Eqs. (M1)-(M16). However, for understanding basic ideas behind inter-chromosome pushing hypothesis and its relevance for spindle mechanics, we provide its simplified version in Box 1.

Choice of parameters. In our model we use 8 parameters, which are either estimated from literature or determined in this study. The Young modulus, $E = 400$ Pa, is taken from⁵², where it corresponds to the extension measurements of mouse embryonic fibroblasts in mitosis. Poisson ratio, $\sigma = 0.3$, is taken as a typical value in⁵³ and corresponds to the extension measurements of newt lung cells in mitosis. DNA density, $\rho = 36$ Mbp/ $\mu\text{m}^3 = 0.037$ pg/ $\mu\text{m}^3 \cdot 978$ Mbp/pg, which has been used only in Fig. 1d, is taken from⁶¹ and corresponds to value obtained for human cells. Spindle length, $L = 14$ μm has been measured in this study. Number of the chromosomes is varied among the values $N = 7, 19, 37, 61, 91$, whereas the value $N = 37$ is used in most of the calculations. Sphere radius is varied from 0.5 μm (0.05 μm for Fig. 3b) to 2 μm , whereas the value $R = 1.25$ μm is used in most of the calculations related to human spindles, to reproduce the observed metaphase plate width with $N = 37$. This radius is slightly larger than the one calculated from human genome size and DNA density, $R = 1.02$ μm , by using Eq. 2 from Box 1. The lattice parameter, $a_0 = 0.25$ μm is chosen to yield the pole diameter of 1.5 μm for $N = 37$, whereas smaller value, $a_0 = 0.0025$ μm , is used in calculations presented in Figs. 1d and 3b, which is necessary to access the width of spindles with small chromosomes. The phenomenological compression coefficient is varied from 0 to 1000 pN/ μm , and value $k = 100$ pN/ μm is chosen in some of the calculations (Fig. 4i, Extended Data Fig. 6a, b and k), to reproduce the observed change in spindle width and height following the compression, with $N = 37$.

Estimation of the relationship between chromosome size and genome size

To apply the model to different species, we need to consider how chromosome shape, size, and number change with the genome size. We chose to obtain these relationships by comparing yeast and human chromosomes because they are well studied and represent small and large genomes, respectively, differing by a factor of 280.

Mitotic chromosomes have a well-defined X-shape with two chromatids each having two arms, where arm length and width is characteristic to species and individual chromosomes. An average mitotic chromatid arm in the yeast *S. cerevisiae* is 0.12 μm wide and around 0.5 μm long, whereas in healthy human RPE1 cells a chromatid arm is 0.65 μm wide and 3 μm long⁶². Thus, both length and width increase by a factor of 5-6, suggesting isometric scaling of typical chromosomes between yeast to humans. This conclusion can be extended to other species based on similar chromosome shapes visible in karyograms of different organisms. Thus, chromosome size of different species can be described by a characteristic length.

To link the characteristic length of a typical chromosome with the species genome size, we assume that the volume of a chromosome, which scales with the characteristic length, is proportional to its number of base pairs. We justify this assumption by the following back-of-the-envelope calculation. The average human chromosome has 3400 Mbp / 23 = 148 Mbp, as the haploid number of chromosomes is 23, and the average yeast chromosome has 12 Mbp / 16 = 0.75 Mbp, as the haploid number of chromosomes is 16, yielding a ratio of 197. Based on our assumption, an average human chromosome has 197 times larger volume than yeast chromosome, implying that characteristic length of human chromosome is $\sqrt[3]{197} = 5.8$ times larger than in yeast. Remarkably, this ratio is within the range of 5-6 obtained from the increase in chromatid arm length and width from yeast to humans described above, supporting our assumption. Thus, the characteristic length of a typical chromosome scales with the 3rd root of genome size.

Cell lines

The cell lines used in this study were: **1.** human hyper-triploid (modal chromosome number = 74)⁹² U2OS (human osteosarcoma, female) cells expressing CENP-A-GFP and mCherry-alpha-tubulin, which were a gift from Helder Maiato (Institute for Molecular Cell Biology, University of Porto, Portugal)⁹³, **2.** human diploid (modal chromosome number = 46)⁹² hTERT-RPE1 (retinal pigmented epithelium, female) cells expressing CENP-A-GFP and centrin1-GFP, which were a gift from Alexey Khodjakov (Wadsworth Center, New York State Department of Health, Albany, NY)⁵⁸, **3.** human diploid hTERT-RPE1 cells and their hypo-tetraploid adapted clones, RPT1, RPT3 and RPT4 (all with modal chromosome number = 80) expressing H2B-GFP, established as described previously³², **4.** human diploid hTERT-RPE1 cells with or without p53 knockdown (KD) expressing H2B-Dendra2, which were a gift from Rene Medema (Netherlands Cancer Institute, Amsterdam, Netherlands)⁹⁴, **5.** Human near-diploid (modal chromosome number = 45) HCT116 (human colorectal carcinoma cell line, male) cells³², and their hypo-tetraploid adapted clones HPT1 (modal chromosome number = 75) and HPT2 (modal chromosome number = 78), established as described previously³².

Cell lines culturing

Cells were cultured in flasks containing Dulbecco's modified Eagle's medium (DMEM; Capricorn Scientific), supplemented with 10% fetal bovine serum (FBS; Sigma-Aldrich) and a 10000 U/mL penicillin/streptomycin solution (Capricorn Scientific). The cultures were maintained at 37°C with 5% CO₂ in a Galaxy 170S CO₂ humidified incubator (Eppendorf) and routinely subcultured upon reaching 70-80% confluence. Prior to experimentation, all cell lines were screened for mycoplasma contamination through monthly assessments using the MycoAlert Mycoplasma Detection Kit (Lonza), and additional checks during imaging procedures with DNA labelling dyes.

Establishment of 3D cultures of mouse primary cells

Mouse small intestine (mSI) organoids were derived from the small intestines of female wild-type C57BL/6 mice, sourced from the Laboratory for Neurodegenerative Disease Research at the Ruđer Bošković Institute, in compliance with the EU Directive 2010/63/EU for animal experimentation and the applicable national regulations of Croatia. The mSI organoids, genetically modified for stable expression of eGFP-Centrin-2, were established using small intestines obtained from mice resulting from crossing of transgenic GFP-CETN2 mice (JAX stock #008234, The Jackson Laboratory)⁹⁵ and transgenic Cre-inducible H2B-mCherry mice (JAX stock #0231239, The Jackson Laboratory)⁹⁶.

To isolate small intestine crypts from mice, the small intestine was cleaned in cold PBS and cut in pieces of 2-5 mm. Cleaned pieces were incubated for 1h in cold 20 mM EDTA in PBS while shaking. Supernatant was collected repeatedly, each collection resulting from incubating the intestine pieces in fresh, cold EDTA solution for 5-10 minutes and passing the agitated suspension through a 70 µm cell strainer. The highest quality collection was centrifuged at 300 g for 7 min at 4°C and the pellet was resuspended in cold PBS. Suspension was mixed with culture medium and Matrigel (Corning) was added in a 1:2 ratio. The final mixture was plated in pre-warmed 24-well plates.

Organoid cultures were maintained in IntestiCult™ Organoid Growth Medium (Mouse, STEMCELL Technologies) and passaging was performed using mechanical fragmentation. For experiments, organoids were dissociated by incubation with TrypLE Express (Thermo Fisher Scientific) for 5 min at 37°C. Dissociated single cells and clumps were plated in Matrigel domes on 35 mm uncoated dishes with 0.17 mm glass thickness (MatTek Corporation), covered with 500 µl of the IntestiCult™ medium and cultured for 24-96h prior to fixation. Samples fixed 24h post-isolation were cultured with addition of 10 µM Y-27632 (ROCK inhibitor, HY-10583, MedChemExpress) and 1h before the fixation the inhibitor was washed out.

Human colorectal cancer organoids

Movies of patient-derived organoids (PDOs), representing various types of colorectal cancer, were partly obtained from a previous study³⁹, while additional movies acquired using the same methods were not included in original publication. The analyzed PDOs included lines established from tumor resections (24Ta, 2Tb, 9T, 7T) and one line derived from healthy tissue adjacent to a tumor (P1N1)³⁹. Additionally, the PDO line P27T, established from a tumor

resection, was excluded from the original publication, but was cultured and imaged under the same conditions as the other PDO lines³⁹.

RNA interference

RPE1 cells 1 day prior to CENP-E depletion, were seeded onto 35 mm glass coverslip dishes with a glass thickness of 0.17 mm (Ibidi) and allowed to reach 50% confluence through incubation. Small interfering RNA (siRNA) constructs were diluted in Opti-MEM medium (Gibco), and transfection was carried out using Lipofectamine RNAiMAX Reagent (Invitrogen) as per the manufacturer's instructions. The ON-TARGETplus Control Pool Non-Targeting pool (D-001810-10-05, Dharmacon) and human CENP-E ON-TARGETplus SMART pool siRNA (L-003252-00-0010, Dharmacon) constructs were used at a final concentration of 100 nM. Following a 4-hour incubation period with the transfection mixture, the medium was replaced with fresh cell culture medium. Fixation subsequent to CENP-E depletion was executed 48 hours after transfection. Depletion effectiveness of used CENP-E siRNAs compared with a non-targeting control was previously measured using the same RNA interference protocol, showing near-total depletion of CENP-E⁹⁷.

Inducing mitosis with unreplicated genome (MUG)

MUG induction in U2OS cells was achieved through incubation with hydroxyurea and caffeine⁴². Stock solutions of hydroxyurea (HY-B0313, MedChemExpress) and caffeine (C0750, Sigma-Aldrich) were prepared at a concentration of 20 mM each. These stock solutions were diluted in DMEM to obtain final concentrations of 2 mM for hydroxyurea and 5 mM for caffeine. U2OS cells were seeded in 2 mL of DMEM at 37°C with 5% CO₂ on 35 mm uncoated glass coverslip dishes (MatTek Corporation). After 12 hours, the culture medium was replaced with 1 mL of DMEM containing 2 mM hydroxyurea, and the cells were incubated for an additional 20 hours. Subsequently, the medium was replaced with fresh medium containing 2 mM hydroxyurea and 5 mM caffeine, and the cells were further incubated for 18 hours before imaging.

Spindle compression assay

The spindle compression method was refined based on previous work⁵⁵, as described in⁶⁰. A solution comprising 2% ultra-pure agarose (#15510, Thermo Fisher Scientific) in PBS was prepared, heated to boiling, and poured into a 35 mm petri dish to solidify, achieving a final thickness of approximately 0.5 cm. During the solidification process, thin strings were inserted into the agarose solution, leaving one end inside the dish while the other remained free outside. Gel areas measuring 1 cm × 1 cm (with strings attached) were excised and stored in PBS at 4°C, then warmed to 37°C immediately before use in experiments. Cells in metaphase were selected from cultures with 80-100% confluence. Following imaging of the metaphase cell before compression, the gel was delicately deposited, centered on the cell. Compression was executed using an oil hydraulic fine manipulator (InjectMan 4, Eppendorf) with a dynamic movement control (100–240 V/50–60 Hz) and a coarse manipulator connected to the confocal Opterra I microscope. A metal rod (part of the micromanipulator) was positioned centrally above the gel, and gradually lowered along the z-axis until gentle contact was made with the

gel (rod diameter significantly larger than cell diameter). The rod was then slowly lowered further (over approximately 10 seconds) by several micrometers until the cell area expanded, as evidenced by the appearance of membrane protrusions. Cell and spindle responses were continuously imaged while maintaining the position of the cell. Subsequently, the cells were imaged for a third time immediately after removing the rod and releasing the pressure. This provided three time points: images before compression, during compression (for 1 minute), and shortly after release. In some instances, cells were left to recover for an extended period to assess their ability to divide before being imaged again. Spindles with a height change of less than 20% during compression were excluded from the analysis.

Induction of mitotic slippage with centrosome elimination

Tetraploid cells were generated from RPE1 cells with p53KD expressing H2B-Dendra2, while hypo-octaploid cells were generated from RPT3 cells expressing H2B-GFP. The cells were seeded in 2 mL of DMEM at 37°C with 5% CO₂ on 35 mm glass coverslip dishes (MatTek Corporation). The following day, the medium was replaced, and fresh DMEM containing the Plk4 inhibitor centrinone³⁴ (HY-18682, MedChemExpress) at a final concentration of 300 nM was added for 24 hours. The following day, the medium was replaced again, and fresh DMEM was replaced sequentially five times. To induce mitotic slippage, cells were treated with 100 μM monastrol (Eg5 inhibitor, HY-101071A, MedChemExpress)⁹⁸ and 500 nM AZ3146 (Mps1 inhibitor, HY-14710, MedChemExpress)⁹⁹ for 24 hours³⁵. Next day, DMEM was replaced five times. After 5 hours, samples were either fixed or subjected to live imaging. Freshly thawed centrinone was exchanged twice a day to prevent Plk4 reactivation and centriole over-duplication. The resulting cell population contained both cells with 1:0 and 1:1 spindles³⁴ (see Extended Data Fig. 2c). To obtain a predominantly population of 1:1 cells, 24 hours after seeding, cells were treated with CDK4/CDK6 inhibitor palbociclib (250 nM, HY-50767, MedChemExpress)¹⁰⁰. The following day, the medium was replaced sequentially five times with fresh DMEM, and cells were simultaneously treated with centrinone, monastrol and AZ3146, in concentrations described above. After 24 hours, the medium was replaced five times with fresh DMEM, and cells were left for 5 hours before imaging or fixation (see Extended Data Fig. 2c).

Induction of cytokinesis failure

Tetraploid RPE1 cells were generated from both p53 wild type and p53 knockdown cells expressing H2B-Dendra. The cells were seeded in 2 mL of DMEM at 37°C with 5% CO₂ on 35 mm glass coverslip dishes (MatTek Corporation). The following day, the cells were treated with either 0.75 μM Cytochalasin D (inhibitor of actin polymerization, HY-N6682, MedChemExpress)¹⁰¹ or 50 μM Blebbistatin (inhibitor of non-muscle myosin II., HY-120870, MedChemExpress)¹⁰², and incubated for 18h overnight. For live cell experiments, the cells were washed four times with 1X PBS and then transferred to the imaging medium. After 6 hours, the cells were taken to the microscope for imaging.

Sample preparation for live cell imaging

Cells were seeded and cultured in DMEM medium with supplements at 37°C and 5% CO₂ on uncoated 35-mm glass coverslip dishes with 0.17-mm (1.5 coverglass) glass thickness (MatTek Corporation). To visualize microtubules in U2OS and RPE1 cells expressing CENP-A-GFP and centrin1-GFP, SPY650-tubulin dye (λ_{Ex} 652 nm, λ_{Em} 674 nm) (Spirochrome AG) was introduced to the dishes at a final concentration of 100 nM, 2-3 hours before imaging. Additionally, for chromosome visualization and determination of mitotic phases, 50 μL of NucBlue Live Ready Probes Reagent (Hoechst 33342) dye (Thermo Fisher Scientific) was added to the dishes 1 minute before imaging.

Live-cell microscopy

The U2OS and hTERT-RPE1 expressing CENP-A-GFP and centrin1-GFP cell lines were imaged using the Bruker Opterra Multipoint Scanning Confocal Microscope¹⁰³ (Bruker Nano Surfaces). The system was mounted on a Nikon Ti-E inverted microscope equipped with a Nikon CFI Plan Apo VC $\times 100/1.4$ numerical aperture oil objective (Nikon). During imaging, cells were maintained at 37°C in an Okolab Cage Incubator (Okolab). A 22 μm slit aperture was used, and the xy-pixel size was set to 83 nm. GFP and mCherry fluorescence were excited using 488 nm and 561 nm diode laser lines, respectively, while SPY dyes were excited using a 640 nm diode laser line. Opterra Dichroic and Barrier Filter Set 405/488/561/640 were employed to separate excitation light from emitted fluorescence. Images were captured with an Evolve 512 Delta EMCCD Camera (Photometrics) with no binning. To cover the entire metaphase spindle, z-stacks were acquired at 30–60 focal planes separated by 0.5 μm using unidirectional xyz scan mode. The system was controlled with Prairie View Imaging Software (Bruker Nano Surfaces).

hTERT-RPE1 parental cells and its post-tetraploid clones expressing H2B-GFP as well as human hTERT-RPE1 cells with or without p53KD and with expression of H2B-Dendra, were imaged using the Lattice Lightsheet 7 system (Zeiss), as described previously⁹⁷. The system was equipped with an illumination objective lens 13.3 \times /0.4 (at a 30° angle to coverglass) with a static phase element and a detection objective lens 44.83 \times /1.0 (at a 60° angle to coverglass) with an Alvarez manipulator. Automatic water immersion was applied from the motorised dispenser at intervals of 20 or 30 minutes. Immediately after sample mounting, the 'create immersion' option was applied four times, followed by 'auto immersion' at 25-minute intervals. The sample was illuminated with a 488 nm diode laser (power output 10 mW) with laser power set to 1-2%. Detection was performed using a Hamamatsu ORCA-Fusion sCMOS camera with an exposure time set to 15-20 ms. The LBF 405/488/561/642 emission filter was used. During imaging, cells were maintained at 37°C with 5% CO₂ in a stage incubation chamber system (Zeiss). The imaging area width in the x dimension was set from 1 to 1.5 mm. Time interval between consecutive frames was set to 2 minutes.

Sample preparation for immunofluorescence

For labelling centrioles and microtubules in RPE-1 cells grown on glass-bottom dishes (14 mm, No. 1.5, MatTek Corporation), a pre-extraction step was carried out with pre-warmed PEM buffer at 37°C (0.1 M PIPES, 0.001 M MgCl₂ \times 6 H₂O, 0.001 M EDTA, 0.5% Triton-X-100)

for 30 seconds at room temperature, followed by fixation with 1 mL of ice-cold methanol for 2 minutes. After fixation, cells underwent three washes of 5 minutes each with 1 mL of PBS and were permeabilized with 0.5% Triton-X-100 solution in water for 30 minutes at room temperature. Subsequently, to block nonspecific binding, cells were incubated in 1 mL of blocking buffer (2% normal goat serum, NGS) for 2 hours at room temperature. After three more washes of 5 minutes each with 1 mL of PBS, cells were incubated with 500 μ l of primary antibody solution overnight at 4°C. Antibody incubation was carried out using a blocking solution composed of 0.1% Triton and 1% NGS in PBS. The following primary antibodies were used: rabbit anti-centrin-3 (1:500, Abcam, ab228690) and rat anti-tubulin (1:500, MA1-80017, Invitrogen). Secondary antibodies used were donkey anti-rabbit Alexa Fluor 647 (1:1000, Abcam, ab150075) and donkey anti-rat Alexa Fluor 594 (1:1000, Abcam, ab150156). Finally, cells underwent three 10-minute washes with 1 mL of PBS before imaging, either immediately or after being stored at 4°C for a maximum period of one week.

For imaging of the mitotic spindle in HCT116-derived cells, the cells were grown on glass-bottomed 96-black well plates and treated with 10 μ M MG132 (Calbiochem) for 3 hours prior to fixation. Cells were briefly washed with PBS, fixed with 100% methanol for 10 min at -20°C, washed three times with PBS, blocked with using 5% FCS/PBS solution with addition of 0.5% TritonX100, incubated overnight with anti- α -tubulin (1:500, Sigma) and anti- γ -tubulin antibody (1:1000, Santa Cruz), washed with 400 mM NaCl and subsequently twice in PBS-T, and detected with DyLight 594- and DyLight 649-conjugated antibodies. DNA was stained with SYTOX Green with added RNase. Cells were finally washed in 400 mM NaCl and twice in PBST.

Organoids were fixed either in warm 4% paraformaldehyde or ice-cold methanol for 1 hour. Subsequent permeabilization, blocking, and staining procedures were performed as described previously¹⁰⁴. Primary antibodies, rabbit anti-centrin-3 (1:300, Abcam, ab228690) and rat anti-tubulin (1:100, MA1-80017, Invitrogen), were diluted in the working buffer and incubated overnight at 4°C. Secondary antibodies used were: donkey anti-rabbit Alexa Fluor 488 or 594 (1:500, Abcam, ab150061, ab150064, respectively) and donkey anti-rat Alexa Fluor 594 (1:500, Abcam, ab150156), which were also incubated overnight at 4°C. Staining with DAPI (1 μ g/mL) and SiR-actin (1 μ M or 2 μ M, Spirochrome) was performed for 20 minutes at room temperature.

Fixed-cell microscopy

All fixed RPE1 cells were imaged by the LSM 800 confocal system (Zeiss) with following parameters: xy sampling, 1.58 μ m; z step size, 0.5 μ m; total number of slices, 26; pinhole, 45-56 μ m; unidirectional scan speed, 10; averaging, 1; 63x Oil DIC f/ELYRA objective (1.4 NA); GaAsP detectors. Laser lines of 405 nm, 561 nm, and 640 nm were used for excitation. Image acquisition was performed using ZEN 3.5 software (blue edition; Zeiss). All fixed HCT116-derived cells were imaged by the Marianas SDC system with inverted Zeiss Observer.Z1 microscope. Following parameters were used: z-step size 0.5 μ m, Plan Apochromat 63x magnification oil objective, with laser lines 473, 561 and 660 nm (LaserStack, Intelligent Imaging Innovations, Inc., spinning disc head (Yokogawa), CoolSNAP-HQ2 and CoolSNAP-EZ CCD cameras (Photometrics, Intelligent Imaging Innovations, Inc.). Image acquisition was performed using SlideBook 5.1.

Confocal microscopy of fixed mSI organoids was conducted using the Expert Line easy3D STED microscope system (Abberior Instruments) with following parameters: 100x/1.4NA UPLSAPO100x oil objective (Olympus) and avalanche photodiode (APD) detector. Laser lines of 405 nm, 488 nm, 561 nm, or 647 nm were utilized for excitation. Image acquisition was performed using the in Inspector software. The xy pixel size was set at 100 nm and 200 nm, and z-stacks were obtained with 500 nm and 2 μ m intervals for individual cells and for whole organoids, respectively.

Measurements of spindle parameters

In cell lines, spindle length was determined in ImageJ from maximum intensity projections (MIPs) or sum-intensity projections of z-stacks of individual cells, as the distance between spindle poles, which were identified as the center of the centriole pair or, if centrioles were absent, as the center of a prominent tubulin signal. Spindle width was defined as the distance between the outermost tubulin-labelled bundles in fixed cells where opposing centrosomes were within 7 μ m in the z-dimension and between the outermost kinetochores in fixed CENP-E-depleted cells. Metaphase plate width and thickness were quantified on MIPs or sum-intensity projections of z-stacks of individual cells in both cell lines and tumor PDOs. Plate width was measured as the distance between the outermost chromosome ends perpendicular to the spindle axis and plate thickness along the spindle axis. These measurements were performed in cells with opposing centrosomes within 7 μ m or 3 μ m in the z-dimension, respectively. Cells with chromosomes in the region between the pole and the metaphase plate and those with multiple polar chromosomes were excluded from plate thickness measurements. Single polar chromosomes were not considered as part of the plate. Angles between poles, discriminated either by centrin signal or center of tubulin signal, and outermost kinetochore fibers were measured using *Angle tool* in ImageJ on MIPs. In freshly generated or naturally present polyploids the metaphase plate thickness and width were measured only in cells where bipolar spindles were formed, evidenced from the clustered centrosomes or a single metaphase plate, and rarely in PDOs when one dominant metaphase plate was formed in a multipolar spindle. The number of metaphase chromosomes in CENP-E depleted cells was determined by subtracting the number of chromosomes outside the metaphase plate from the total number of chromosomes in diploid human cells ($2n = 46$), based on kinetochore signals. Nuclear area was assessed in ImageJ using the polygon selection tool on MIPs or sum-intensity projections of z-stacks of individual cells. For live-imaged cells, nuclear area was measured a few hours before nuclear envelope breakdown (NEBD), while in fixed cells, it was measured in prophase cells with condensed DNA. Spindle height was measured in ImageJ as the distance between the first and last z-frame showing tubulin signal. This measurement was corrected by multiplying the obtained spindle height by a factor of 0.81 to account for refractive index mismatch⁸⁷.

In mouse primary cells, analyzed cells in metaphase comprised either single cells or portions of early organoid formations from the 2-cell stage onwards. Only multicellular structures lacking the characteristic asymmetric aspect ratios seen in mature organoids undergoing apical mitosis were considered. Selection criteria were based on nuclear and chromosome positioning relative to actin-labelled cell boundaries in images of complete organoid structures. Metaphase cells were categorized into two groups: diploid or polyploid,

determined by the presence of either 2 or more Centrin-2 or Centrin-3 pairs, respectively. Spindle width, metaphase plate thickness, and diameter were quantified as described for cell lines. Spindle length was measured as the three-dimensional distance between opposing centrosomes or midpoint positions of centrosome clusters, as indicated by the centrin signal. Except for spindle length ($p = 0.025$), there were no significant differences observed in diploid or polyploid groups between cells fixed with methanol or paraformaldehyde, thus they are collectively presented. Across all parameters, no significant differences were noted within diploid or polyploid groups between cells derived from Centrin-2-labelled or unlabeled organoids, or between cells originating from organoids treated or untreated with the ROCK inhibitor, hence they are represented together.

Metaphase plate width and spindle length in acentriolar cells were measured from published images using ImageJ, with the scale bar serving as the distance guide. Comparisons were limited to cells processed and imaged using the same protocols, including live-imaged human oocytes, mouse embryonic cells, and mouse and human oocytes fixed by the same methods, as referenced in Extended Data Table 2. For HAP1 cells, data were obtained from representative examples of naturally present near-haploid and near-diploid subpopulations, as detailed in the reference provided in Extended Data Table 2.

Image processing, data analysis and statistics

Image analysis was performed in Fiji/ImageJ (National Institutes of Health) and plotting was done in Python (The Python Software Foundation) and MatLab (MathWorks). For plotting univariate scatter plots, Matlab “UnivarScatter” extension was used (<https://github.com/manulera/UnivarScatter>). Raw images were used for quantification. Figures were composed in Adobe Illustrator CS5 (Adobe Systems). In Fig. 2b (top), diploid and hypo-tetraploid groups contain both DMSO- and centrinone-treated cells. In Extended Data Fig. 2f, all groups contain both 1:0 and 1:1 spindles, while Fig. 2b (bottom) contains only 1:1 spindles, as the number of centrioles significantly influences only spindle length (see Extended Data Fig. 4a-c). In Fig. 2c and Extended Data Fig. 3a, the tetraploid group contains both cells generated by cytokinesis failure and mitotic slippage whereas the diploid group contains both H2B-Dendra2 and H2B-GFP expressing RPE1 cells.

Bioinformatics analysis of gene expression data from diploid RPE1 and post-tetraploid RPT clones³² was performed in R/Bioconductor using “limma” for normalization and differential expression analysis. Log₂ expression ratios (RPT compared to RPE1) were calculated for each gene. Processed RNA sequencing data were analyzed using Pathway Analysis, with “fdrtool” for false discovery rate correction and “ggplot2” for visualization. Genes were filtered using UniProt identifiers to focus on kinesin superfamily proteins (KIFs), spindle assembly factors, and MAPs, guided by GOCC terms.

The p values when comparing two independent classes were obtained using the independent Student’s t -test (significance level was 5%). The p values when comparing multiple classes were obtained using the one-way ANOVA test followed by Tukey’s Honest Significant Difference (HSD) test (significance level was 5%). The p values and z -score when comparing the difference between two dependent correlations with one variable in common were obtained using Steiger’s correlation Z -test¹⁰⁵ (significance level was 5%). No statistical methods were used to predetermine the sample size. The experiments were not randomized

and, except where stated, the investigators were not blinded to allocation during experiments and outcome evaluation.

Acknowledgements

We thank Alexey Khodjakov, Helder Maiato, and Rene Medema for providing cell lines; the Laboratory for Neurodegenerative Disease Research led by Silva Katušić at the Ruder Bošković Institute for assistance with isolation of mouse small intestine; Ivana Šarić for the illustrations and assembling the figures; and members of the Tolić and Pavin groups for their constructive comments on the manuscript. This work was funded by the European Research Council (ERC-SyG 855158, I.M.T., N.P., and G.J.P.L.K.); the Croatian Science Foundation projects (HRZZ IP-2019-04-5967, N.P.; HRZZ IP-2022-10-1091, M.LJ. and J.T.; HRZZ IP-2024-05-5336, I.M.T.) and Swiss-Croatian Bilateral Project (IPCH-2022-10-9344, I.M.T.); projects co-financed by the Croatian Government and the European Union through the European Regional Development Fund—the Competitiveness and Cohesion Operational Programme IPSted (KK.01.1.1.04.0057, I.M.T.) and QuantiXLie Center of Excellence (KK.01.1.1.01.0004, N.P. and I.M.T.); and the Deutsche Krebshilfe (Project 70115224, Z.S.).

Contributions

Analysis of spindle scaling across eukaryotes was conceptualized and carried out by I.M.T. and N.P., with help from K.V. and L.G. Experiments on RPE1 cells across ploidies were performed and analyzed by L.G., K.V., and A.P., with help in analysis from L.P. Transcriptome analysis and HCT116 movies were done by A-L.H. and Z.S. Patient-derived organoid movies from G.J.P.L.K.'s lab were prepared by T.V.R. and analyzed by K.V. Primary mouse cell experiments were carried out by I.D. on organoids established by Ma.T. CENP-E experiments were conducted by K.V. and analyzed by L.P. Compression and MUG experiments were performed by Mo.T. and L.G. Theoretical model was designed by N.P. with help from M.N., J.T., and M.LJ., and solved by J.T., M.LJ., and M.N. The manuscript was written by I.M.T. and N.P. with help from K.V., L.G., and M.N., and feedback from all authors.

Data availability

All relevant data supporting the findings of this study are provided within the article and its Extended Data files. Raw images used in this work are available from the corresponding authors upon reasonable request.

Code availability

The code for the numerical computations of the theoretical model is available at <https://github.com/matkec0/spindleFEM>.

Competing interests

The authors declare no competing interests.

References

1. Marshall, W. F. Scaling of Subcellular Structures. *Annu. Rev. Cell Dev. Biol.* **36**, 219–236 (2020).
2. Alberts, B. *et al.* *Molecular Biology of the Cell*. (W. W. Norton & Company, New York, NY London, 2022).
3. Gregory, T. R. *et al.* Eukaryotic genome size databases. *Nucleic Acids Res.* **35**, D332–D338 (2007).
4. Santaguida, S. & Amon, A. Short- and long-term effects of chromosome mis-segregation and aneuploidy. *Nat. Rev. Mol. Cell Biol.* **16**, 473–485 (2015).
5. Helmke, K. J., Heald, R. & Wilbur, J. D. Interplay Between Spindle Architecture and Function. *Int. Rev. Cell Mol. Biol.* **306**, 83–125 (2013).
6. Crowder, M. E. *et al.* A Comparative Analysis of Spindle Morphometrics across Metazoans. *Curr. Biol.* **25**, 1542–1550 (2015).
7. Decker, F., Oriola, D., Dalton, B. & Brugués, J. Autocatalytic microtubule nucleation determines the size and mass of *Xenopus laevis* egg extract spindles. *eLife* **7**, e31149 (2018).
8. Wühr, M. *et al.* Evidence for an Upper Limit to Mitotic Spindle Length. *Curr. Biol.* **18**, 1256–1261 (2008).
9. Krüger, L. K. & Tran, P. T. Spindle scaling mechanisms. *Essays Biochem.* **64**, 383–396 (2020).
10. Valdez, V. A., Neahring, L., Petry, S. & Dumont, S. Mechanisms underlying spindle assembly and robustness. *Nat. Rev. Mol. Cell Biol.* **24**, 523–542 (2023).
11. Good, M. C., Vahey, M. D., Skandarajah, A., Fletcher, D. A. & Heald, R. Cytoplasmic Volume Modulates Spindle Size During Embryogenesis. *Science* **342**, 856–860 (2013).
12. Hazel, J. *et al.* Changes in Cytoplasmic Volume Are Sufficient to Drive Spindle Scaling. *Science* **342**, 853–856 (2013).
13. Rieckhoff, E. M. *et al.* Spindle Scaling Is Governed by Cell Boundary Regulation of Microtubule Nucleation. *Curr. Biol.* **30**, 4973–4983.e10 (2020).
14. Wilbur, J. D. & Heald, R. Mitotic spindle scaling during *Xenopus* development by kif2a and importin α . *eLife* **2**, e00290 (2013).
15. Lacroix, B. *et al.* Microtubule Dynamics Scale with Cell Size to Set Spindle Length and Assembly Timing. *Dev. Cell* **45**, 496–511.e6 (2018).
16. Greenan, G. *et al.* Centrosome Size Sets Mitotic Spindle Length in *Caenorhabditis elegans* Embryos. *Curr. Biol.* **20**, 353–358 (2010).
17. Zhou, C. Y. *et al.* Mitotic chromosomes scale to nuclear-cytoplasmic ratio and cell size in *Xenopus*. *eLife* **12**, e84360 (2023).
18. Hara, Y. & Kimura, A. An allometric relationship between mitotic spindle width, spindle length, and ploidy in *Caenorhabditis elegans* embryos. *Mol. Biol. Cell* **24**, 1411–1419 (2013).
19. Kletter, T. *et al.* Volumetric morphometry reveals spindle width as the best predictor of mammalian spindle scaling. *J. Cell Biol.* **221**, e202106170 (2021).
20. Miller, K. E., Cadart, C. & Heald, R. Dodecaploid *Xenopus longipes* provides insight into the emergence of size scaling relationships during development. *Curr. Biol.* **33**, 1327–1336.e4 (2023).

21. Dinarina, A. *et al.* Chromatin Shapes the Mitotic Spindle. *Cell* **138**, 502–513 (2009).
22. Gaetz, J., Gueroui, Z., Libchaber, A. & Kapoor, T. M. Examining how the spatial organization of chromatin signals influences metaphase spindle assembly. *Nat. Cell Biol.* **8**, 924–932 (2006).
23. Gan, L., Ladinsky, M. S. & Jensen, G. J. Organization of the Smallest Eukaryotic Spindle. *Curr. Biol.* **21**, 1578–1583 (2011).
24. Risteski, P., Jagric, M., Pavin, N. & Tolic, I. M. Biomechanics of chromosome alignment at the spindle midplane. *Curr Biol* **31**, R574–R585 (2021).
25. Maiato, H., Gomes, A. M., Sousa, F. & Barisic, M. Mechanisms of Chromosome Congression during Mitosis. *Biology (Basel)* **6**, (2017).
26. Matkovic, J. *et al.* Kinetochore- and chromosome-driven transition of microtubules into bundles promotes spindle assembly. *Nat. Commun.* **13**, 7307 (2022).
27. Gibcus, J. H. *et al.* A pathway for mitotic chromosome formation. *Science* **359**, eaao6135 (2018).
28. Wilkins, B. J. *et al.* A Cascade of Histone Modifications Induces Chromatin Condensation in Mitosis. *Science* **343**, 77–80 (2014).
29. Schneider, M. W. G. *et al.* A mitotic chromatin phase transition prevents perforation by microtubules. *Nature* **609**, 183–190 (2022).
30. Cuylen, S. *et al.* Ki-67 acts as a biological surfactant to disperse mitotic chromosomes. *Nature* **535**, 308–312 (2016).
31. Kelleher, C. P., Rana, Y. P. & Needleman, D. J. Long-range repulsion between chromosomes in mammalian oocyte spindles. *Sci. Adv.* **10**, eadq7540 (2024).
32. Kuznetsova, A. Y. *et al.* Chromosomal instability, tolerance of mitotic errors and multidrug resistance are promoted by tetraploidization in human cells. *Cell Cycle* **14**, 2810–2820 (2015).
33. Cohen-Sharir, Y. *et al.* Aneuploidy renders cancer cells vulnerable to mitotic checkpoint inhibition. *Nature* **590**, 486–491 (2021).
34. Wong, Y. L. *et al.* Reversible centriole depletion with an inhibitor of Polo-like kinase 4. *Science* **348**, 1155–60 (2015).
35. Gemble, S. *et al.* Genetic instability from a single S phase after whole-genome duplication. *Nature* **604**, 146–151 (2022).
36. Ganem, N. J., Godinho, S. A. & Pellman, D. A mechanism linking extra centrosomes to chromosomal instability. *Nature* **460**, 278–282 (2009).
37. Potapova, T. A., Seidel, C. W., Box, A. C., Rancati, G. & Li, R. Transcriptome analysis of tetraploid cells identifies cyclin D2 as a facilitator of adaptation to genome doubling in the presence of p53. *Mol. Biol. Cell* **27**, 3065 (2016).
38. Dürubaum, M. *et al.* Unique features of the transcriptional response to model aneuploidy in human cells. *BMC Genom.* **15**, 139 (2014).
39. Bolhaqueiro, A. C. F. *et al.* Ongoing chromosomal instability and karyotype evolution in human colorectal cancer organoids. *Nat. Genet.* **51**, 824–834 (2019).
40. de Medeiros, G. *et al.* Multiscale light-sheet organoid imaging framework. *Nat. Commun.* **13**, 4864 (2022).
41. Yaguchi, K. *et al.* Uncoordinated centrosome cycle underlies the instability of non-diploid somatic cells in mammals. *J. Cell Biol.* **217**, 2463–2483 (2018).

42. Wise, D. A. & Brinkley, B. R. Mitosis in cells with unreplicated genomes (MUGs): spindle assembly and behavior of centromere fragments. *Cell Motil. Cytoskeleton* **36**, 291–302 (1997).
43. Holubcová, Z., Blayney, M., Elder, K. & Schuh, M. Error-prone chromosome-mediated spindle assembly favors chromosome segregation defects in human oocytes. *Science* **348**, 1143–1147 (2015).
44. So, C. *et al.* A liquid-like spindle domain promotes acentrosomal spindle assembly in mammalian oocytes. *Science* **364**, eaat9557 (2019).
45. Roeles, J. & Tsiavaliaris, G. Actin-microtubule interplay coordinates spindle assembly in human oocytes. *Nat. Commun.* **10**, 4651 (2019).
46. Wu, T. *et al.* Mechanisms of minor pole-mediated spindle bipolarization in human oocytes. *Science* **385**, eado1022 (2024).
47. Baumann, C., Wang, X., Yang, L. & Viveiros, M. M. Error-prone meiotic division and subfertility in mice with oocyte-conditional knockdown of pericentrin. *J. Cell Sci.* **130**, 1251–1262 (2017).
48. Mihalas, B. P. *et al.* Age-dependent loss of cohesion protection in human oocytes. *Curr. Biol.* **34**, 117-131.e5 (2024).
49. Somfai, T. *et al.* Diploid porcine parthenotes produced by inhibition of first polar body extrusion during in vitro maturation of follicular oocytes. *Reproduction* **132**, 559–570 (2006).
50. Paim, L. M. G. & FitzHarris, G. Tetraploidy causes chromosomal instability in acentriolar mouse embryos. *Nat. Commun.* **10**, 4834 (2019).
51. Poirier, M. G. & Marko, J. F. Mitotic chromosomes are chromatin networks without a mechanically contiguous protein scaffold. *Proc. Natl. Acad. Sci. U.S.A.* **99**, 15393–15397 (2002).
52. Liu, N., Qiang, W., Jordan, P., Marko, J. & Qiao, H. Cell-cycle and Age-Related Modulations in Mouse Chromosome Stiffness. 2024.03.06.583771 Preprint at <https://doi.org/10.1101/2024.03.06.583771> (2024).
53. Houchmandzadeh, B., Marko, J. F., Chatenay, D. & Libchaber, A. Elasticity and Structure of Eukaryote Chromosomes Studied by Micromanipulation and Micropipette Aspiration. *J. Cell Biol.* **139**, 1–12 (1997).
54. Pavin, N. & Tolic, I. M. Mechanobiology of the Mitotic Spindle. *Dev. Cell* **56**, 192–201 (2021).
55. Dumont, S. & Mitchison, T. J. Compression regulates mitotic spindle length by a mechanochemical switch at the poles. *Curr. Biol.* **19**, 1086–95 (2009).
56. Jiang, J.-W., Kim, S. Y. & Park, H. S. Auxetic nanomaterials: Recent progress and future development. *Appl. Phys. Rev.* **3**, 041101 (2016).
57. Itabashi, T. *et al.* Probing the mechanical architecture of the vertebrate meiotic spindle. *Nat. Methods* **6**, 167–172 (2009).
58. Magidson, V. *et al.* The spatial arrangement of chromosomes during prometaphase facilitates spindle assembly. *Cell* **146**, 555–67 (2011).
59. Goshima, G., Wollman, R., Stuurman, N., Scholey, J. M. & Vale, R. D. Length Control of the Metaphase Spindle. *Curr. Biol.* **15**, 1979–1988 (2005).

60. Trupinić, M. *et al.* The chirality of the mitotic spindle provides a mechanical response to forces and depends on microtubule motors and augmin. *Curr. Biol.* **32**, 2480-2493.e6 (2022).
61. Kramer, E. M., Tayjasanant, P. A. & Cordone, B. Scaling Laws for Mitotic Chromosomes. *Front. Cell Dev. Biol.* **9**, (2021).
62. Kakui, Y. *et al.* Chromosome arm length, and a species-specific determinant, define chromosome arm width. *Cell Rep.* **41**, 111753 (2022).
63. Cisneros-Soberanis, F. *et al.* Near millimolar concentration of nucleosomes in mitotic chromosomes from late prometaphase into anaphase. *J. Cell Biol.* **223**, e202403165 (2024).
64. Davidson, I. F. & Peters, J.-M. Genome folding through loop extrusion by SMC complexes. *Nat. Rev. Mol. Cell Biol.* **22**, 445–464 (2021).
65. Seto, E. & Yoshida, M. Erasers of Histone Acetylation: The Histone Deacetylase Enzymes. *Cold Spring Harb. Perspect Biol.* **6**, a018713 (2014).
66. Paulson, J. R., Hudson, D. F., Cisneros-Soberanis, F. & Earnshaw, W. C. Mitotic chromosomes. *Semin. Cell Biol.* **117**, 7–29 (2021).
67. Kajtez, J. *et al.* Overlap microtubules link sister k-fibres and balance the forces on bi-oriented kinetochores. *Nat. Commun.* **7**, 10298 (2016).
68. Nicklas, R. B. Measurements of the force produced by the mitotic spindle in anaphase. *J Cell Biol* **97**, 542–8 (1983).
69. Ye, A. A., Cane, S. & Maresca, T. J. Chromosome biorientation produces hundreds of piconewtons at a metazoan kinetochore. *Nat. Commun.* **7**, 13221 (2016).
70. Lancaster, O. M. *et al.* Mitotic Rounding Alters Cell Geometry to Ensure Efficient Bipolar Spindle Formation. *Dev. Cell* **25**, 270–283 (2013).
71. Cattin, C. J. *et al.* Mechanical control of mitotic progression in single animal cells. *Proc. Natl. Acad. Sci. U.S.A.* **112**, 11258–11263 (2015).
72. Bastianello, G. *et al.* Mechanical stress during confined migration causes aberrant mitoses and c-MYC amplification. *Proc. Natl. Acad. Sci. U.S.A.* **121**, e2404551121 (2024).
73. Cadart, C., Zlotek-Zlotkiewicz, E., Le Berre, M., Piel, M. & Matthews, H. K. Exploring the Function of Cell Shape and Size during Mitosis. *Dev. Cell* **29**, 159–169 (2014).
74. Sazer, S., Lynch, M. & Needleman, D. Deciphering the Evolutionary History of Open and Closed Mitosis. *Curr. Biol.* **24**, R1099–R1103 (2014).
75. Kalinina, I. *et al.* Pivoting of microtubules around the spindle pole accelerates kinetochore capture. *Nat. Cell Biol.* **15**, 82–87 (2013).
76. Suresh, P., Long, A. F. & Dumont, S. Microneedle manipulation of the mammalian spindle reveals specialized, short-lived reinforcement near chromosomes. *eLife* **9**, e53807 (2020).
77. Koprivec, I., Štimac, V., Mikec, P. & Tolić, I. M. Microtubule pivoting driven by spindle elongation rescues polar chromosomes to ensure faithful mitosis. 2024.06.16.599200 Preprint at <https://doi.org/10.1101/2024.06.16.599200> (2024).
78. Courtois, A., Schuh, M., Ellenberg, J. & Hiiragi, T. The transition from meiotic to mitotic spindle assembly is gradual during early mammalian development. *J. Cell Biol.* **198**, 357–370 (2012).

79. Hara, Y., Iwabuchi, M., Ohsumi, K. & Kimura, A. Intranuclear DNA density affects chromosome condensation in metazoans. *Mol. Biol. Cell* **24**, 2442–2453 (2013).
80. Ono, Y. *et al.* Shape of the first mitotic spindles impacts multinucleation in human embryos. *Nat. Commun.* **15**, 5381 (2024).
81. Fluks, M., Milewski, R., Tamborski, S., Szkulmowski, M. & Ajduk, A. Spindle shape and volume differ in high- and low-quality metaphase II oocytes. *Reproduction* **167**, e230281 (2024).
82. Storchová, Z. *et al.* Genome-wide genetic analysis of polyploidy in yeast. *Nature* **443**, 541–547 (2006).
83. Mitchison, T. J. *et al.* Roles of Polymerization Dynamics, Opposed Motors, and a Tensile Element in Governing the Length of *Xenopus* Extract Meiotic Spindles. *Mol. Biol. Cell* **16**, 3064–3076 (2005).
84. Duncan, A. W. *et al.* The ploidy conveyor of mature hepatocytes as a source of genetic variation. *Nature* **467**, 707–710 (2010).
85. Vitale, I. *et al.* Illicit survival of cancer cells during polyploidization and depolyploidization. *Cell Death Differ.* **18**, 1403–1413 (2011).
86. Van de Peer, Y., Mizrahi, E. & Marchal, K. The evolutionary significance of polyploidy. *Nat. Rev. Genet.* **18**, 411–424 (2017).
87. Novak, M. *et al.* The mitotic spindle is chiral due to torques within microtubule bundles. *Nat. Commun.* **9**, 3571 (2018).
88. Landau, L. D. & Lifshits, E. M. *Theory of Elasticity*. vol. 7 (Pergamon, Oxford, 1959).
89. Tutek, Z. & Aganović, I. A justification of the one-dimensional linear model of elastic beam. *Math. Methods Appl. Sci.* **8**, 502–515 (1986).
90. Grubišić, L. & Tambača, J. Direct solution method for the equilibrium problem for elastic stents. *Numer. Linear Algebra Appl.* **26**, e2231 (2019).
91. Čanić, S., Grubišić, L., Ljulj, M., Maretić, M. & Tambača, J. Geometric optimization of vascular stents modeled as networks of 1D rods. *J. Comput. Phys.* **494**, 112497 (2023).
92. Truong, M. A. *et al.* A kinesin-based approach for inducing chromosome-specific mis-segregation in human cells. *EMBO J.* **42**, e111559 (2023).
93. Barisic, M. *et al.* Microtubule detyrosination guides chromosomes during mitosis. *Science* **348**, 799–803 (2015).
94. Soto, M., García-Santisteban, I., Krenning, L., Medema, R. H. & Raaijmakers, J. A. Chromosomes trapped in micronuclei are liable to segregation errors. *J. Cell Sci.* **131**, jcs214742 (2018).
95. Higginbotham, H., Bielas, S., Tanaka, T. & Gleeson, J. G. Transgenic Mouse Line with Green-fluorescent Protein-labeled Centrin 2 allows Visualization of the Centrosome in Living Cells. *Transgenic Res.* **13**, 155–164 (2004).
96. Peron, S. P., Freeman, J., Iyer, V., Guo, C. & Svoboda, K. A Cellular Resolution Map of Barrel Cortex Activity during Tactile Behavior. *Neuron* **86**, 783–799 (2015).
97. Vukušić, K. & Tolić, I. M. CENP-E initiates chromosome congression by opposing Aurora kinases to promote end-on attachments. 2023.10.19.563150 Preprint at <https://doi.org/10.1101/2023.10.19.563150> (2024).
98. Mayer, T. U. *et al.* Small Molecule Inhibitor of Mitotic Spindle Bipolarity Identified in a Phenotype-Based Screen. *Science* **286**, 971–974 (1999).

99. Hewitt, L. *et al.* Sustained Mps1 activity is required in mitosis to recruit O-Mad2 to the Mad1–C-Mad2 core complex. *J. Cell Biol.* **190**, 25–34 (2010).
100. Scott, S. J., Suvarna, K. S. & D’Avino, P. P. Synchronization of human retinal pigment epithelial-1 cells in mitosis. *J. Cell Sci.* **133**, jcs247940 (2020).
101. Flanagan, M. D. & Lin, S. Cytochalasins block actin filament elongation by binding to high affinity sites associated with F-actin. *J. Biol. Chem.* **255**, 835–838 (1980).
102. Straight, A. F. *et al.* Dissecting Temporal and Spatial Control of Cytokinesis with a Myosin II Inhibitor. *Science* **299**, 1743–1747 (2003).
103. Buđa, R., Vukusic, K. & Tolic, I. M. Dissection and characterization of microtubule bundles in the mitotic spindle using femtosecond laser ablation. *Methods Cell Biol.* **139**, 81–101 (2017).
104. Fatehullah, A., Appleton, P. L. & Näthke, I. S. Cell and tissue polarity in the intestinal tract during tumorigenesis: cells still know the right way up, but tissue organization is lost. *Philos. Trans. R. Soc. B* **368**, 20130014 (2013).
105. Lee, I. A. & Preacher, K. J. Calculation for the test of the difference between two dependent correlations with one variable in common [Computer software]. (2013).

Box 1

Model for spindle scaling

The aim of the model is to identify general biomechanical principles common to spindles of different architectures across eukaryotes. Thus, we use the simplest description of the key spindle components: (i) chromosomes are elastic spheres with a volume corresponding to that of a typical chromosome for a species, (ii) microtubules attached to a chromosome are described as a flexible rod passing through the chromosome. The core assumption of our model is that each chromosome is squeezed by the pushing force from a neighboring chromosome,

$$F = -ch^{3/2}, \quad (1)$$

where h describes how much the centers of two neighboring spheres approach each other from the undeformed state (Fig. 3a)⁸⁸. The elasticity constant, $c = \frac{1}{3}E\sqrt{2R}/(1 - \sigma^2)$, is given for sphere radius, R , Young's modulus, E , and Poisson's ratio, σ . Based on our comparison of yeast and human chromosome size, we assume that the chromosome volume, $V = \frac{4\pi}{3}R^3$, depends on the genome size, G , chromosome number, N , and the DNA density, ρ ,

$$V = \frac{G}{N\rho}, \quad (2)$$

from which we calculate radius of the spheres for different species (Methods). The radii of all chromosomes within a species are identical, as well as the number of chromosomes in all species, because both parameters vary up to 10-fold, considerably less than the genome size across the species (Fig. 1).

Each chromosome experiences repulsive force arising from interaction with all of its neighbors,

$$\mathbf{F}_{\text{chr}} = \sum_{\text{neighbors}} \hat{\mathbf{r}}F. \quad (3)$$

where $\hat{\mathbf{r}}$ is the unit vector along the line connecting sphere centers. This force pushes the central part of the associated microtubule outwards, while being balanced by the forces keeping the microtubule ends in place at the left and right spindle pole, $\mathbf{F}_{\text{chr}} + \mathbf{F}_{\text{left}} + \mathbf{F}_{\text{right}} = 0$. These forces lead to the bending of the microtubule bundle, of flexural rigidity κ and extending in the xy -plane, according to the Euler-Bernoulli beam equation,

$$\frac{d^2y}{dx^2} = -\frac{F_{\text{chr}}x}{2\kappa}, \quad (4)$$

for the left half of the microtubule bundle, where we use a small angle approximation and $F_{\text{chr}} = |\mathbf{F}_{\text{chr}}|$. While this box provides insight into the main concepts behind our theory, a complete formulation of the model is given in Methods. It includes all chromosomes and their microtubules, whose ends are connected to two spindle poles, and the case of external compression of the spindle.

Main figures with legends

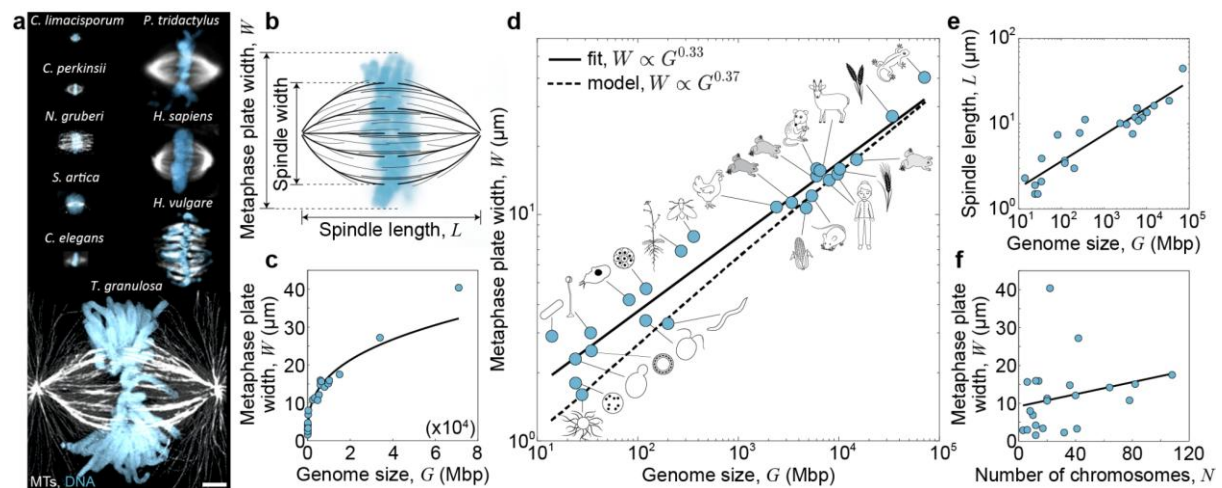


Figure 1. Metaphase plate width shows a power-law scaling with the genome size across eukaryotes. **a**, Spindles with labelled DNA (blue) and microtubules (grey) in denoted eukaryotic species, adapted from^{18,19,106–109}. **b**, A scheme of measured spindle geometrical parameters. **c**, **d**, Metaphase plate width, W , as a function of genome size, G , for a set of eukaryotes (schematically depicted in **d**, $n = 25$) on a linear (**c**) and log-log scale (**d**), from **Extended Data Table 1** (note that these eukaryotes vary in the open versus closed mode of mitosis, the spindle pole structure, and the kinetochore organization, as detailed in **Extended Data Fig. 1a**). The solid line shows a power-law fit, $W \propto G^{0.33}$, and the dashed line is the extrapolation of the model for parameter values for human cells (Methods) and the DNA density $\rho = 36 \text{ Mbp}/\mu\text{m}^3$ ⁶¹, where a fit yields $W \propto G^{0.37}$. **e**, Spindle length, L , as a function of the genome size, for the same species as in panel (**d**), and a power-law fit with an exponent $L \propto G^{0.31}$, $R^2 = 0.85$, $p = 10^{-11}$. **f**, Metaphase plate width as a function of chromosome number, N , for the $n = 22$ species from (**d**), and a linear fit, $R^2 = 0.06$, $p = 0.26$.

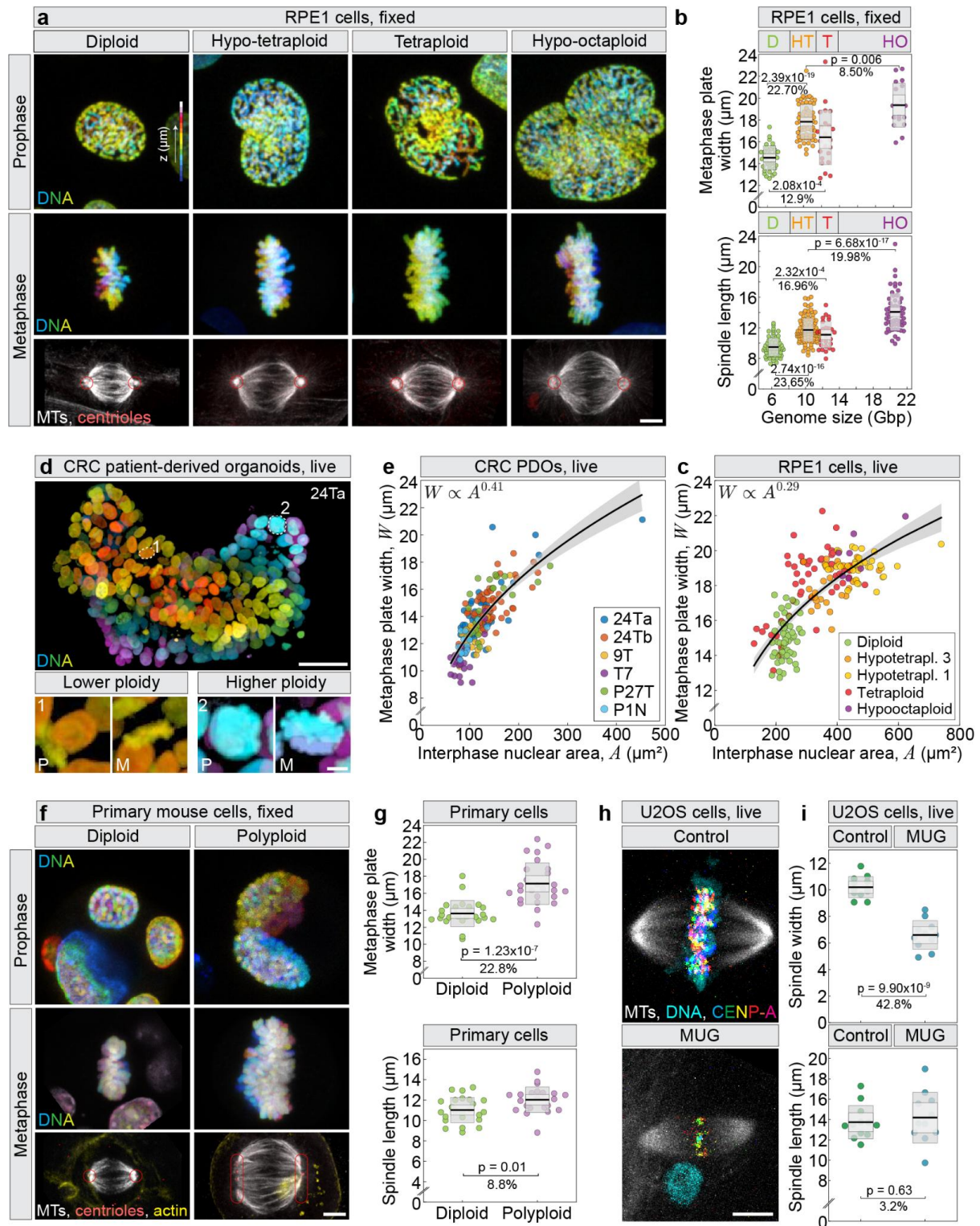


Figure 2. Sublinear scaling of metaphase plate width with ploidy in differentiated cells, primary cells, and patient-derived organoids. **a, f** DNA in RPE1 (**a**) and primary mouse (**f**) cells of different ploidy expressing H2B (**a**) or labelled with DAPI (**f**) during prophase (top) and metaphase (middle), with immunostaining for α -tubulin (MTs, grey), centrin-3 (centrioles, red, encircled) (**a, f**) and SiR-actin labelling (actin, yellow) (**f**) (bottom). **b**, Metaphase plate width (top) and spindle length (bottom) measured in cells with varying genome sizes, estimated from the diploid human genome (6.27 Gbp). Number of cells: 36, 59, 23, 18 (top); 65, 113, 28, 60 (bottom). **c, e**, Metaphase plate width, W , versus interphase nuclear area, A , in RPE1 cells

of different ploidies (**c**), and in colorectal cancer (CRC) patient-derived organoids (PDOs) lines (**e**) with a power-law relationship ($W \propto A^{0.29}$, $R^2 = 0.57$, $p = 2.57 \times 10^{-31}$), and ($W \propto A^{0.41}$, $R^2 = 0.63$, $p = 3.21 \times 10^{-25}$), respectively, and 95% confidence intervals. Number of cells: 58, 28, 36, 51, 7 (**c**); 58, 59, 21, 27, 23 (**e**). **d**, CRC PDOs expressing H2B (top), with cells of lower (1) and higher (2) ploidy enlarged (bottom). Movies obtained from³⁹. **g**, Metaphase plate width (top) and spindle length (bottom) in primary mouse cells of different ploidy. Number of cells: 26, 26 (top); 24, 22 (bottom). **h**, U2OS cells expressing CENP-A and α -tubulin (MTs) during control mitosis (top) and mitosis with an unreplicated genome (MUG, bottom), with spindle width (top) and length (bottom) quantified for both conditions (**i**). Number of cells: 12, 11 (top); 12, 11 (bottom). DNA and CENP-A are color-coded for depth. Abbreviations: D, diploid; HT, hypotetraploid; T, tetraploid; HO, hypooctaploid; P, prophase; M, metaphase; Hypoterapl. 1, hypotetraploid clone RPT1; Hypoterapl. 3, hypotetraploid clone RPT3. Scale bars, 5 μ m. **b**, **g** and **i**, data are mean with 95% confidence intervals and standard deviation. **b**, Tukey's HSD. **g**, **i**, Student's t-test. Each panel includes data from at least three independent experiments.

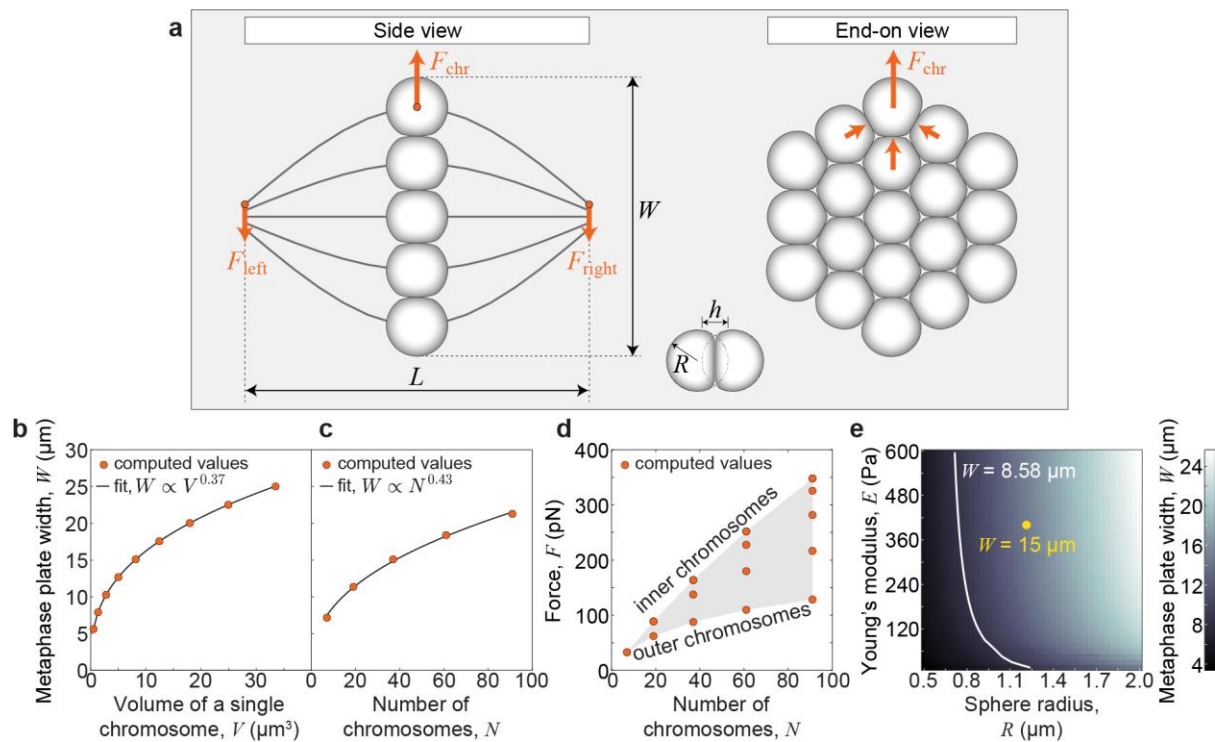


Figure 3. Physical model of the metaphase plate. **a**, Geometry of the metaphase spindle (spindle length, L and metaphase plate width, W) with 19 chromosomes (deformed spheres) and forces exerted on the individual microtubule bundle (black line), F_{left} , F_{right} and F_{chr} , shown in the side view (left) and end-on view (right). Force at the chromosome, F_{chr} , arises from the repulsion of its nearest neighbours. Positions of spheres are calculated by the model, whereas their deformations are schematically represented, see example of two spheres in contact with labelled reduction in distance between the sphere centres, h , and the radius of each sphere, R . **b**, Metaphase plate width versus the volume of the single chromosome and the fit. The value of lattice parameter is $a_0 = 0.0025 \mu\text{m}$. **c**, Metaphase plate width versus the chromosome number and the fit. **d**, Inter-chromosome pushing force versus the chromosome number calculated as the total force exerted by 3 inner neighbors, as depicted in (a). **e**, Phase diagram of metaphase plate width as a function of the chromosome's Young's modulus versus chromosome radius. The yellow dot depicts parameter values used in panel (c), and the white line shows values of R and E yielding $W = 8.58 \mu\text{m}$. If not stated otherwise, parameter values are: Young's modulus $E = 400 \text{ Pa}$, Poisson ratio $\sigma = 0.3$, $N = 37$, $L = 14 \mu\text{m}$, $R = 1.25 \mu\text{m}$, and $a_0 = 0.25 \mu\text{m}$.

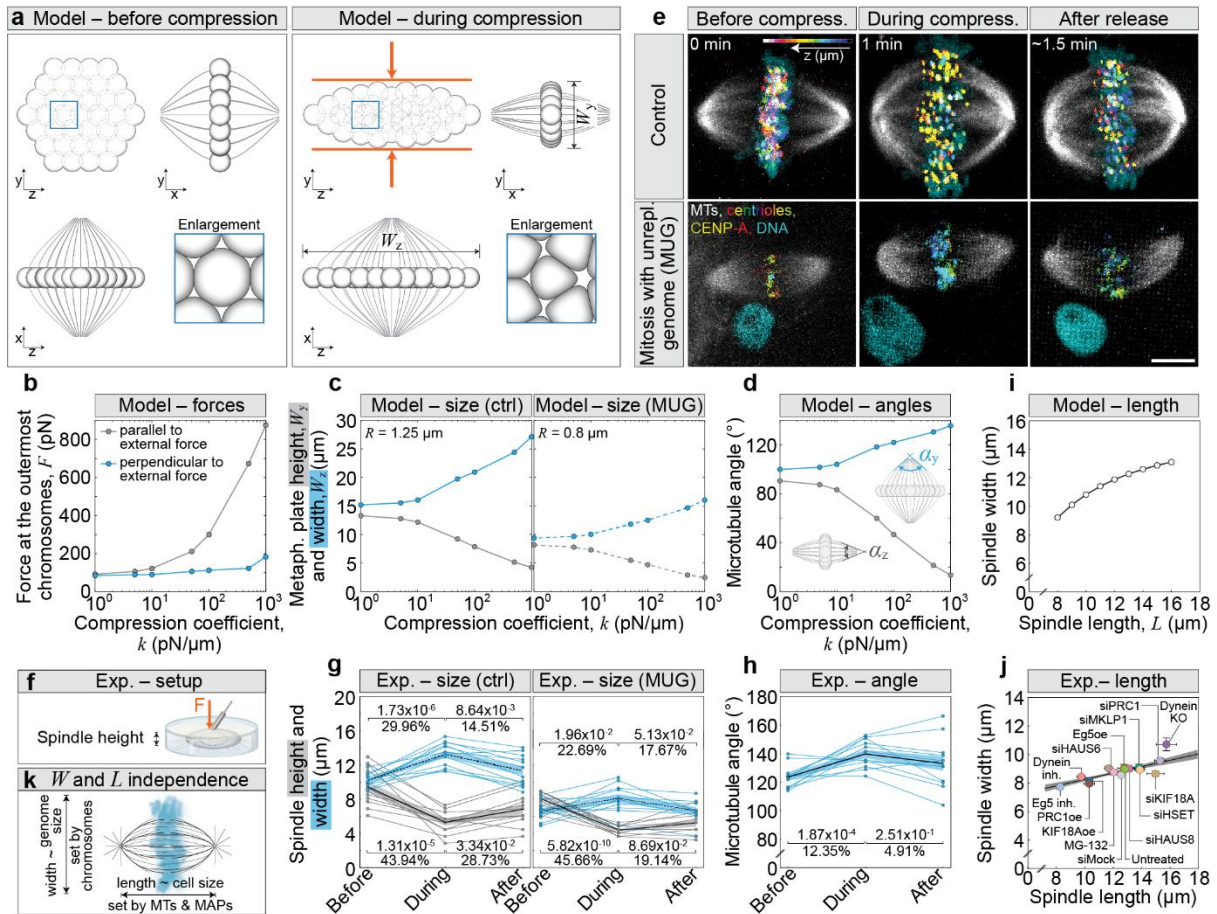


Figure 4. Inter-chromosome pushing forces within the metaphase plate cause spindle expansion. **a**, Examples of two solutions of the model without (left) and with (right) the external force exerted at the chromosomes, depicted by red arrows. Solutions are shown in the end-on view (upper left), and two side views (upper right, metaphase plate width in y direction, W_y , and lower left, metaphase plate width in z direction, W_z). **b**, Inter-chromosome pushing force at the outermost chromosomes, at $y = 0$ and $z = 0$. **c**, Model prediction for the metaphase plate width and height under compression for two different sphere radii. **d**, Two microtubule angles (see schemes) at the pole under compression. **e**, Spindles before, during and after compression in live-imaged U2OS cells expressing CENP-A (color-coded for depth) and α -tubulin (MTs, grey) with labelled DNA (cyan) in control (top) and mitosis with unreplicated genome (MUG, bottom) cells. **f**, Setup for spindle compression. **g**, Spindle height (grey) and spindle width (cyan) before, during and after compression for control (left) and MUG (right) cells. **h**, Angle between pole and outermost kinetochore fiber for three time points related to compression of U2OS control cells. Thick lines, mean; shaded areas, standard error of the mean (SEM); thin lines, individual cells. Number of cells: 12 (g, left and h); 11 (g, right). **i**, Model prediction of spindle width, $W - 2R$, for different spindle lengths. **j**, Mean \pm SEM for spindle width versus spindle length for protein perturbation experiments. Data from⁶⁰. Black line, linear fit ($R^2 = 0.58$, $p = 1.41 \times 10^{-25}$ grey area, 95% confidence interval). **k**, Spindle width (W) is determined by the chromosomes and scales with their size. Spindle length (L) is set by microtubules and microtubule-associated proteins (MAPs), and scales with the cell size. In (b)-(d) and (i) parameters are as in Fig. 3, unless stated otherwise. Abbreviations: Unrepl., unreplicated; Compress., compression; ctrl, control; Exp., experiment; MTs, microtubules; oe, overexpression; si, small interfering; KO, knock-out; inh., inhibition. The number of cells equals the number of independent experiments **e**, Student's t-test.

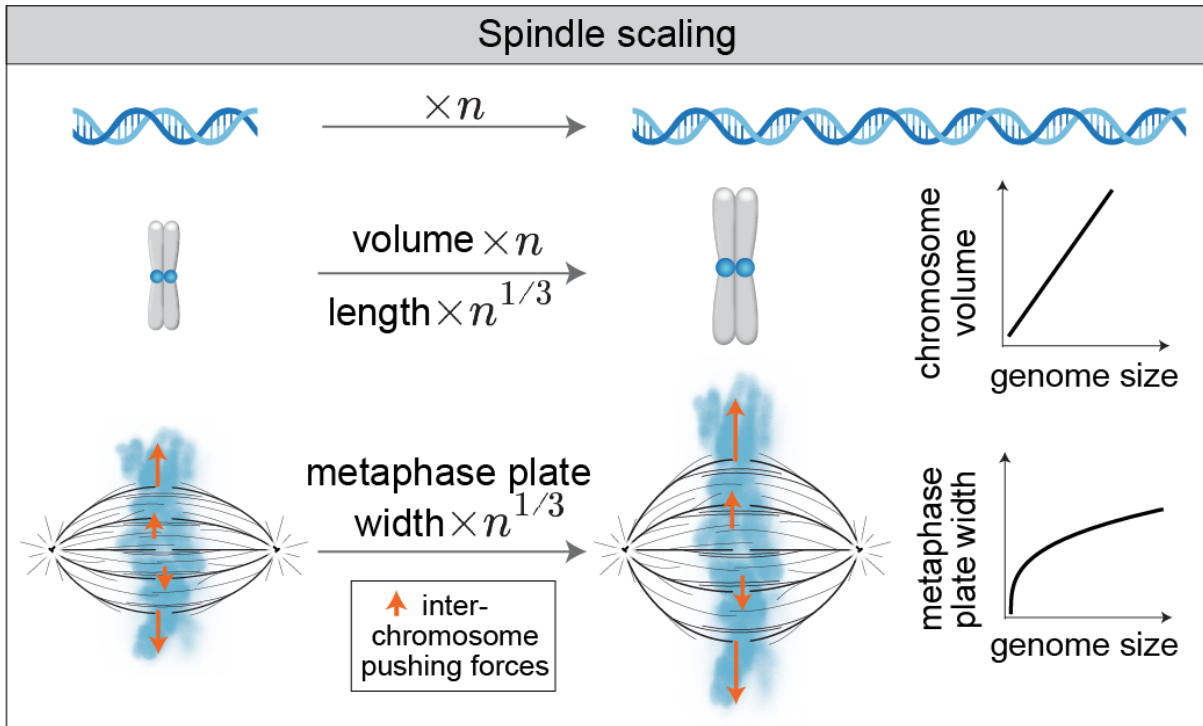
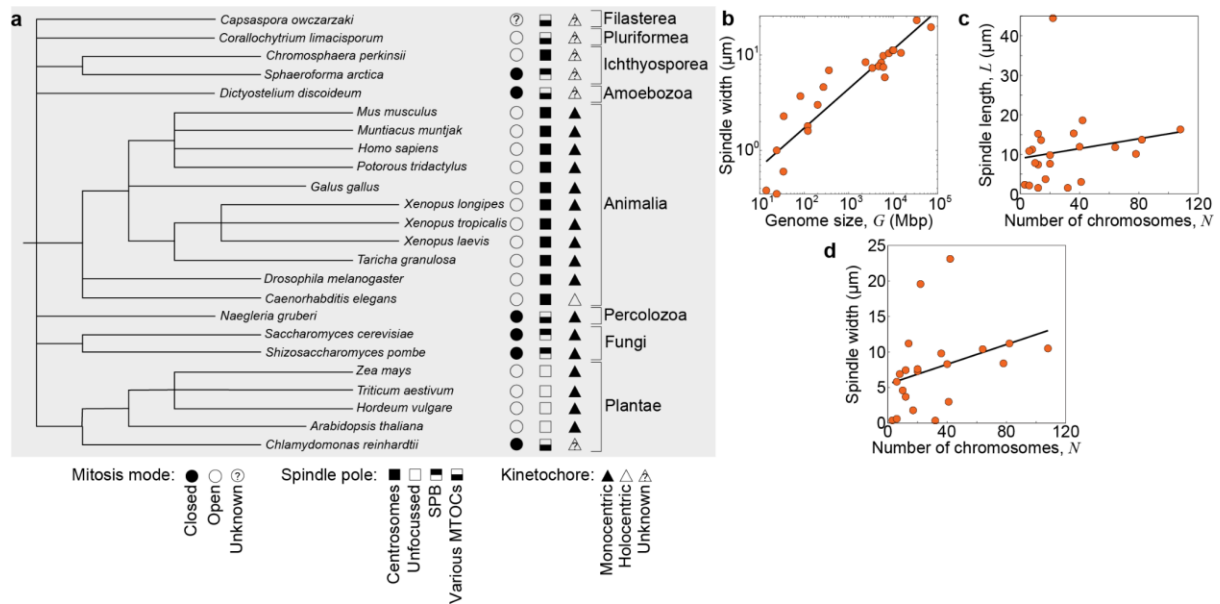


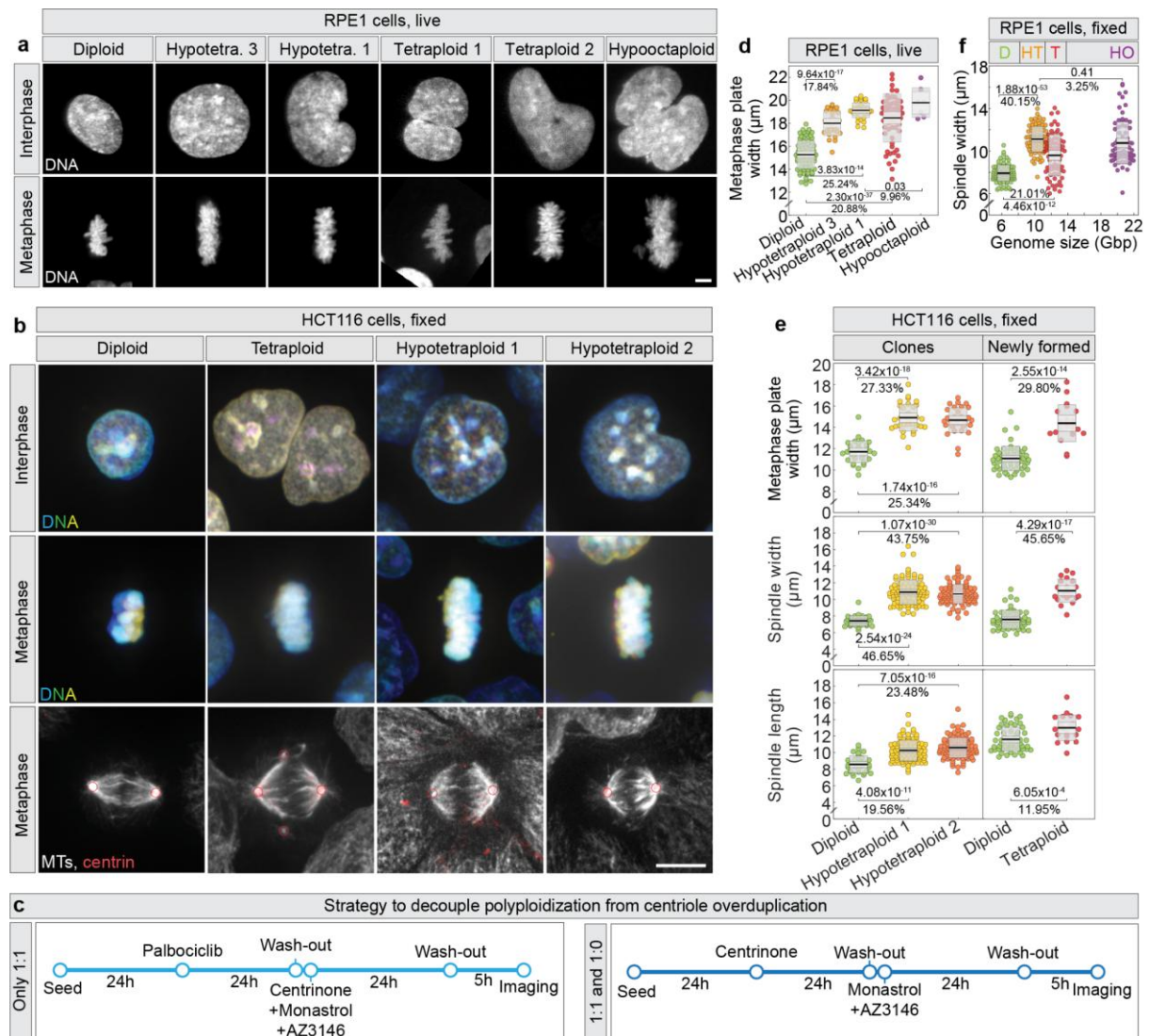
Figure 5. Chromosome crowding in the metaphase plate sets the scaling of the mitotic spindle with the genome size. When DNA length increases n times, the volume of a typical chromosome also increases n times, while its length and the metaphase plate width increase only $n^{1/3}$ times. Thus, a significant change in genome size requires only a small variation in spindle size. The mechanism of spindle adaptation to varying genome sizes is based on spindle widening due to inter-chromosome pushing forces (arrows).

Extended Data

Extended Data figures and tables with legends

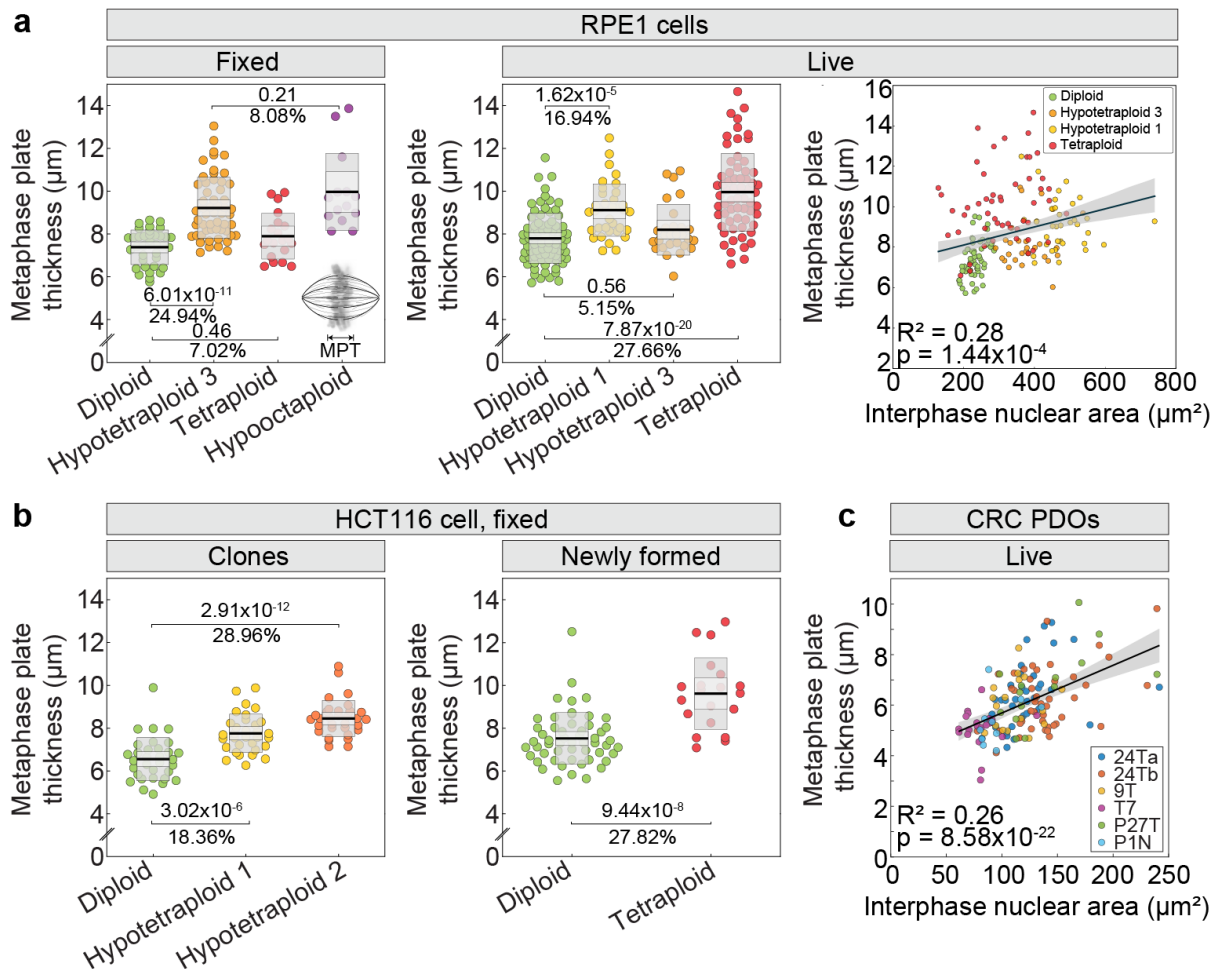


Extended Data Figure 1. Phylogenetic tree of eukaryotic species used in the study and their mitotic spindle parameters versus number of chromosomes or genome size. **a**, A phylogenetic tree based on the NCBI taxonomy, including species from Extended Data Table 1, with eukaryotic kingdoms, clades, or phyla denoted on the right. Schemes representing various modes of mitosis (circles), spindle pole organization (squares), and kinetochore structure (triangles) are shown according to the legend at the bottom. **b**, Spindle width as a function of the genome size for the same species as in Figure 1d, and a power-law fit with an exponent $W \propto G^{0.41}$, $R^2 = 0.85$, $p = 10^{-10}$. **c**, Spindle length, L , as a function of the chromosome number, N , for the same species as in Figure 1d, and a linear fit, $R^2 = 0.04$, $p = 0.39$. **d**, Spindle width as a function of the chromosome number, N , for the same species as in Figure 1d, and a linear fit, $R^2 = 0.12$, $p = 0.12$. Abbreviations: SPB, spindle pole body, MTOCs, microtubule-organizing centers.

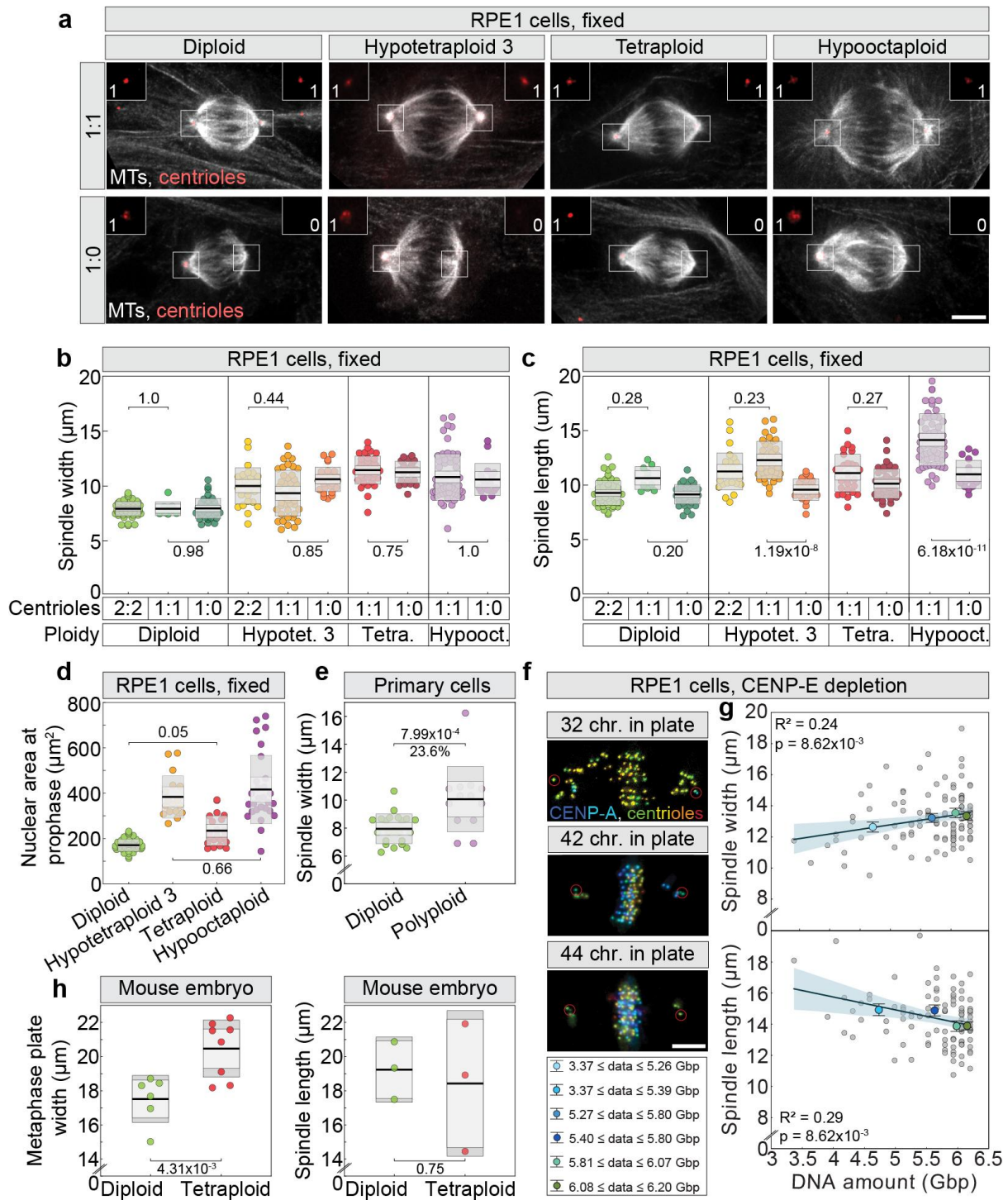


Extended Data Figure 2. The scaling of spindle dimensions with ploidy in human differentiated cells is determined by the amount of DNA in the metaphase plate. **a**, DNA in live-imaged RPE-1 cells of different ploidy levels stably expressing H2B-Dendra2 or H2B-GFP at interphase (top row) and last frame before anaphase (bottom row). **b**, DNA (color-coded for depth) in fixed HCT116 cells of different ploidy levels in interphase (top) and metaphase (middle). HCT116 cells of different ploidy levels in metaphase immunostained for α -tubulin (MTs, gray) and centrin-3 (centrioles, red, encircled) (bottom). DNA was stained with DAPI. **c**, Protocols to generate polyploid cells without centriole overduplication, targeting two outcomes: cells with one centriole per centrosome (1:1, left) or a mixture of cells with one centriole per centrosome (1:1) and cells with only a single centriole (1:0) (right). Exact concentrations are detailed in the Methods. **d**, Metaphase plate width across live-imaged RPE1 cells of different ploidy levels. **e**, Metaphase plate width (top), spindle width (middle) and spindle length (bottom) for fixed hypo-tetraploid HCT116 clones and their diploid controls (left), and newly formed tetraploids with their internal diploid controls (right). **f**, Spindle width across fixed RPE1 cells with different ploidy levels. Percentages on (d), (e) and (f) represent differences from the mean values, the thick black line shows the mean; the light and dark gray areas mark 95% confidence interval on the mean and standard deviation, respectively; p values from (Tukey's HSD test) are given in (d), (e, left) and (f); p values from (Student's t-test) are given in (e, right). Number of cells - (a) 40, 17, 21, 28; (d) 82, 36, 28, 63, 7; (e) 32, 32, 32, 54, 20 (top); 32, 96, 100, 54, 20 (middle);

32, 96, 100, 54, 20 (bottom); (f) 100, 68, 86, 75. Each group is a pool of at least three independent experiments. Abbreviations: Hypotetra. 1, hypotetraploid clone RPT1; Hypotetra. 3, hypotetraploid clone RPT3; Tetraploid 1, tetraploid cell generated by cytokinesis failure; Tetraploid 2, tetraploid cell generated by mitotic slippage; Hypotetraploid 1, hypotetraploid clone HPT1; Hypotetraploid 3, hypotetraploid clone HPT3; D, diploid; HT, hypotetraploid; T, tetraploid; HO, hypooctaploid. All scale bars, 5 μm .

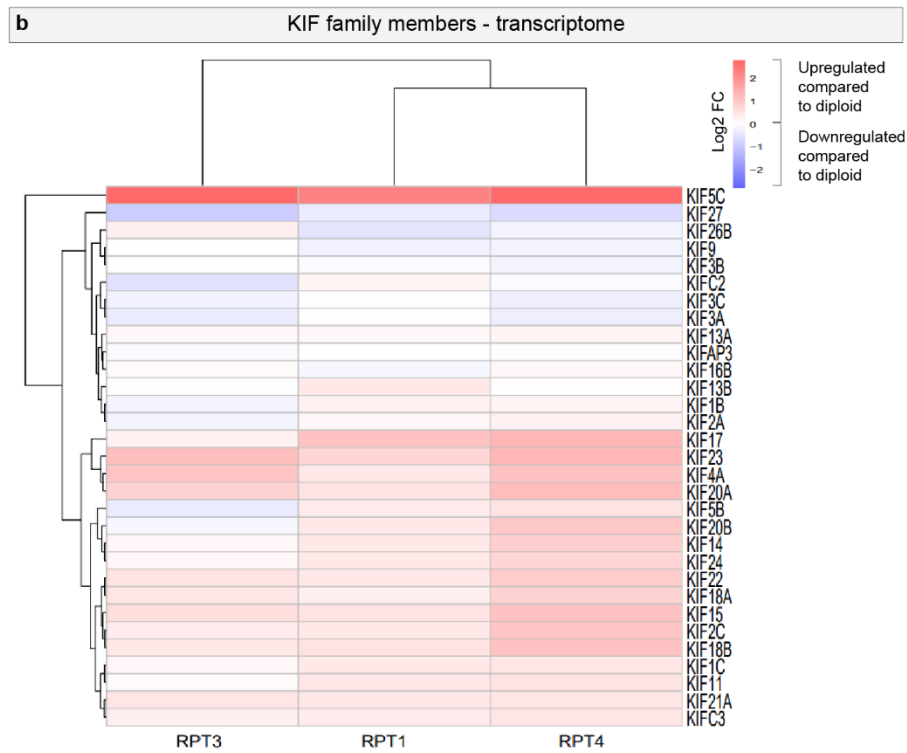
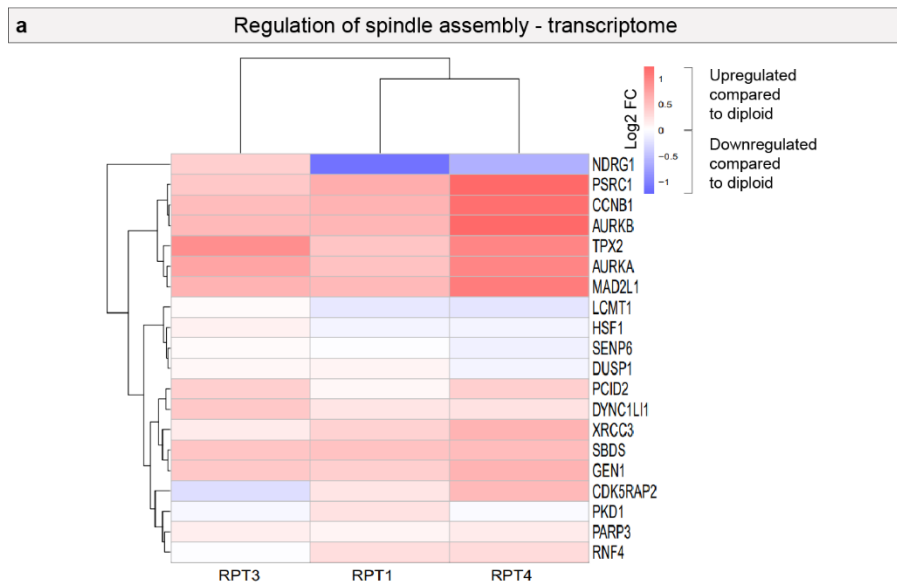


Extended Data Figure 3. Metaphase plate thickness increases with increasing ploidy in human differentiated cells and colorectal patient-derived organoids. **a**, Metaphase plate thickness (MPT) for RPE1 cells of different ploidy. Fixed cells (left), live cells (middle). The scheme of MPT measurement is shown in the left graph. Metaphase plate thickness versus interphase nuclear area for live-imaged RPE1 cells (right) of different ploidy for conditions as indicated in the legend. Black line represents mean linear fit; shaded area, 95% confidence interval. Metaphase plate thickness for live-imaged RPE1 cells was measured at a frame before anaphase onset. Hypotetraploids 1 and 3 represent clones RPT1 and RPT3. **b**, Metaphase plate thickness for fixed hypotetraploid HCT116 clones HTP1 and HPT2 and their diploid controls (left), and newly formed tetraploids with their internal diploid controls (right). **c**, Metaphase plate thickness versus interphase nuclear area of cells from live-imaged colorectal cancer (CRC) patient derived organoids (PDOs) across multiple lines (legend). On (a, left and middle) and (b) the black line shows the mean; the light and dark gray areas mark 95% confidence intervals on the mean and standard deviation, respectively. In (a, right) and (c), lines represent mean linear fit; shaded areas, 95% confidence interval. P values in (a, left and middle) are given from (Tukey's HSD test), in (a, right) and (c) from (Wald test) and in (b) from (Student's t test). Number of cells - (a) 37, 55, 20, 14 (left); 82, 36, 28, 63 (middle); 58, 28, 36, 51 (right); (b) 32, 32, 32 (left); 54, 20 (right); (c) 35, 44, 17, 20, 14, 10. Each group is a pool of at least three independent experiments.

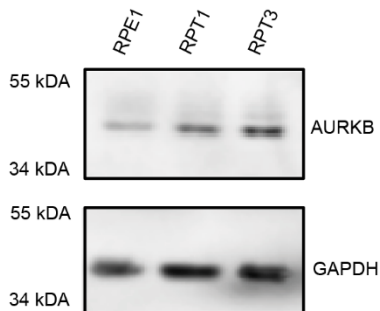


Extended Data Figure 4. Number of centrosomes impacts spindle length, but not spindle width across ploidies in differentiated cells. **a**, RPE1 cells of different ploidies immunostained for α -tubulin (MTs, grey) and centrin-3 (centrioles, red, encircled). First row represents spindles with one centriole on each centrosome (1:1) and the bottom row represents spindles with only one centriole (1:0). Zoomed views of the centrosome area (boxed) are located in the upper corners. **b** and **c**, Spindle width (**b**) and spindle length (**c**) across different ploidies and different number of centrioles. The black line shows the mean; the light and dark gray areas mark 95% confidence intervals on the mean and standard deviation, respectively. **d**, Nuclear area at prophase across different ploidies for fixed RPE1 cells. **e**, Spindle width across primary mouse cells of different ploidy. **f**, RPE1 cells stably expressing CENP-A-GFP (CENP-

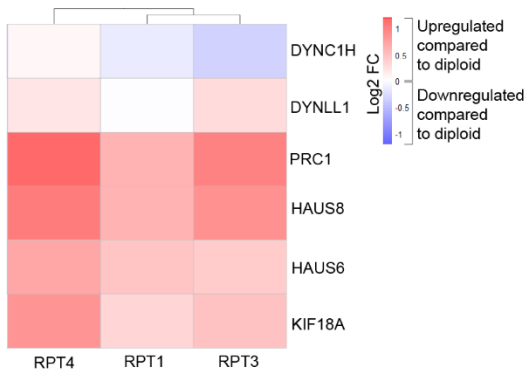
A), and centrin-3-GFP (centrioles, encircled) color coded for depth, after depletion of CENP-E, with indicated number of chromosomes in the metaphase plate. **g**, Spindle width (top) and spindle length (bottom) versus DNA amount in metaphase plate for RPE-1 cells fixed after CENP-E depletion with mean \pm standard error of the mean (SEM) for conditions as indicated in the legend. The DNA amount was determined by multiplying the total genomic DNA by the number of chromosomes retained in the metaphase plate. Black line, linear fit; blue area, 95% confidence interval. **h**, Metaphase plate width (left) and spindle length (right) for diploid and tetraploid mouse acentriolar blastocysts. Data is measured from published images⁵⁰. P values (Tukey's HSD test) are given in (b), (c) and (d); p values from (Student's T-test) are given in (e) and (h); p values from (Wald test) are given in (g). Abbreviations: Hypotet. 3, hypotetraploid clone RPT3; Tetra., tetraploid; Hypooct., hypooctaploid; chr., chromosomes. All scale bars, 5 μ m. Number of cells - (b) 55, 9, 36, 27, 38, 21, 28, 40, 60, 16; (c) 55, 10, 41, 27, 38, 22, 28, 43, 63, 16; (d) 40, 17, 21, 28; (e) 22, 13; each group is a pool of at least three independent experiments; (g) 115 (top), 105 (bottom) contain data from 2 independent experiments.



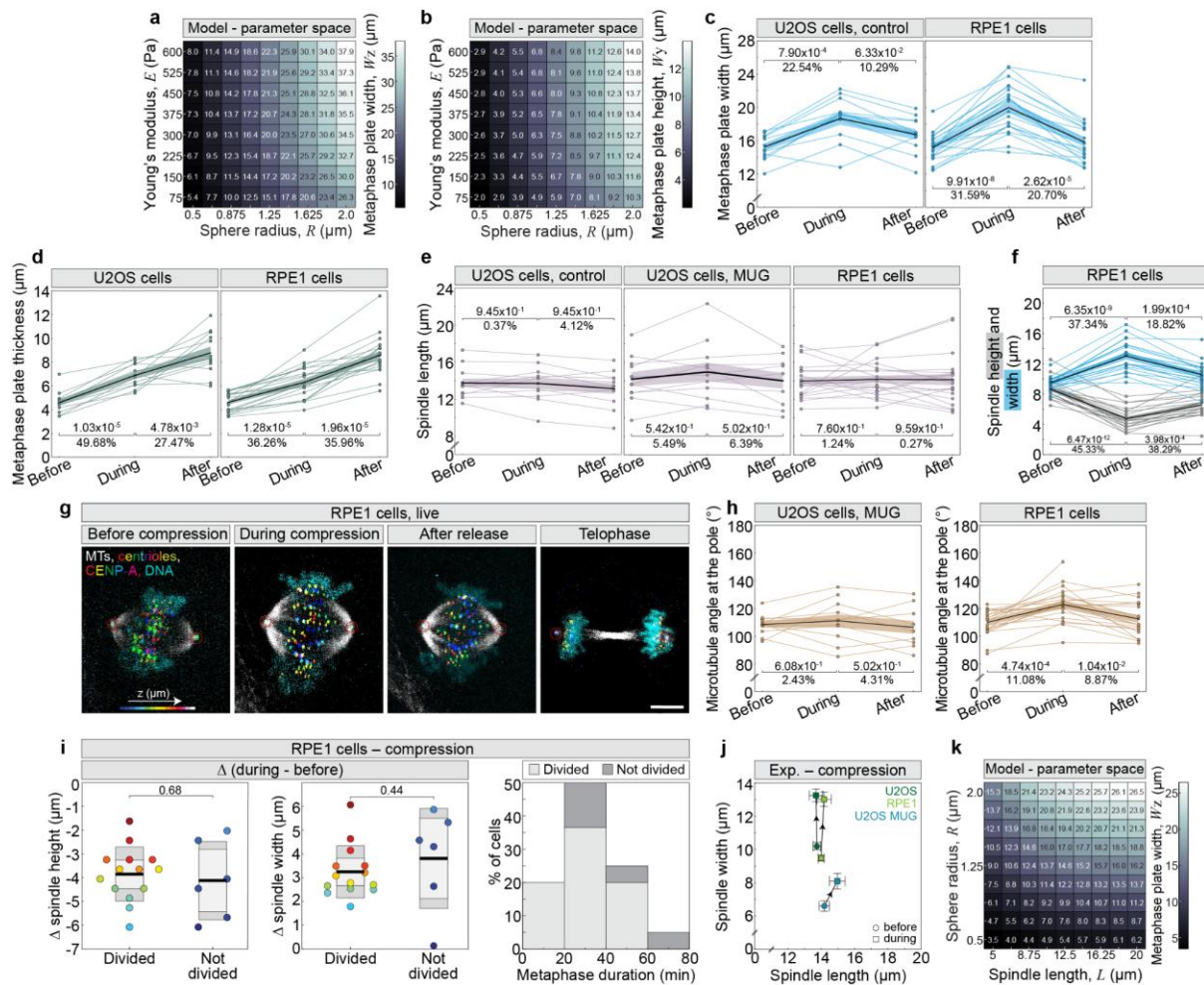
c AURKB western blot



d Selected MAPs - transcriptome

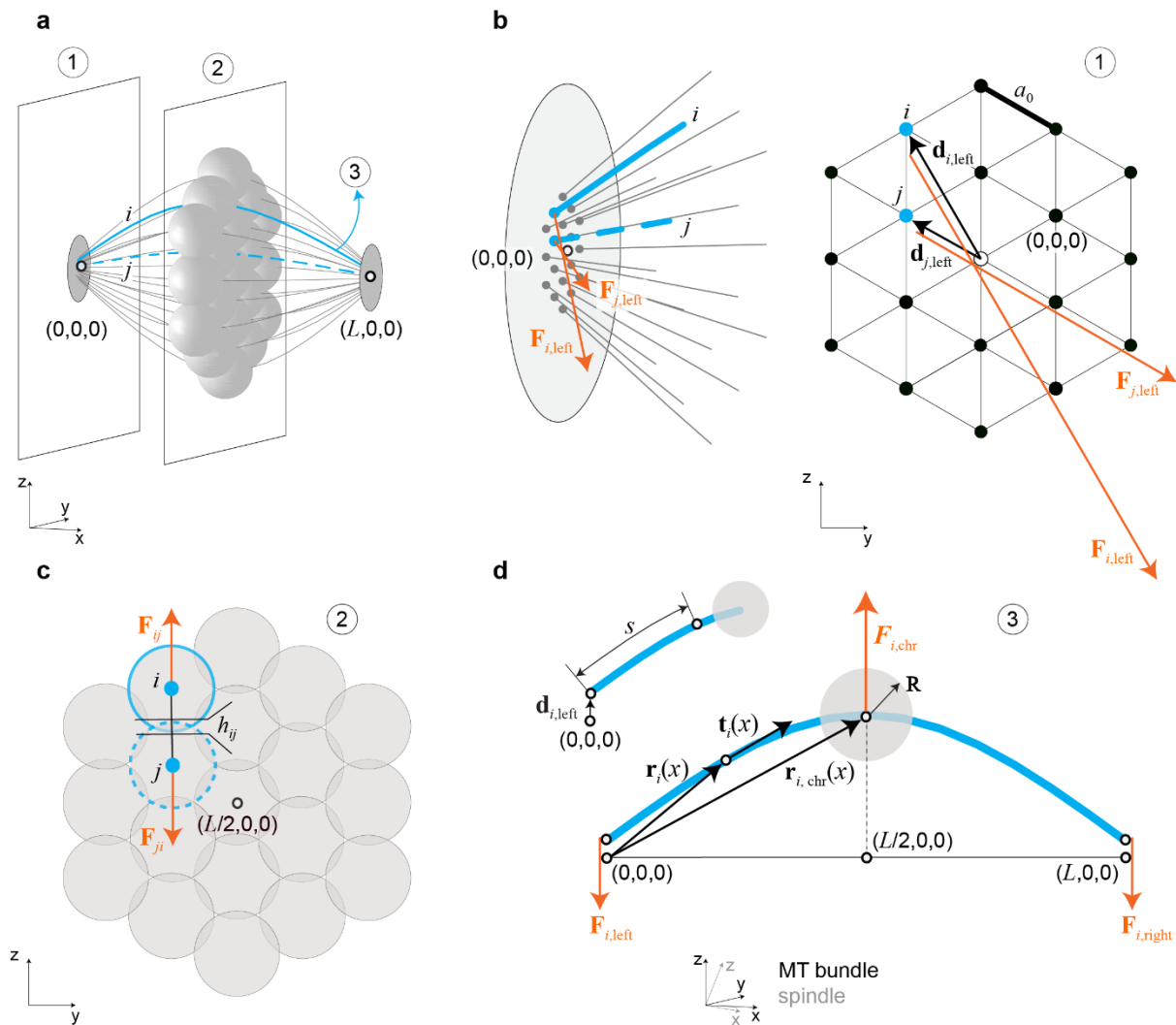


Extended Data Figure 5. Transcriptome analysis of adapted tetraploid clones reveals substantial changes in the expression of mitotic factors compared to the diploid cells. a, Comparison of genes involved in spindle assembly in hypotetraploid RPE1 (RPT) cell lines and their diploid parental wild type counterparts. Genes significantly upregulated (red) and downregulated (blue) are shown (FDR < 0.05). FC, fold change. **b,** Expression changes in genes of the kinesin (KIF) family from post-tetraploid cell lines compared to the diploid parental wild type. GOCC annotation highlights the functional relevance of these changes, with significantly upregulated (red) and downregulated (blue) genes indicated (FDR < 0.05). GOCC annotation was employed to identify functional pathways. **c,** Immunoblot analysis of lysates from indicated cell lines. Antibody against Aurora B (AURKB) was used to estimate protein level, with glyceraldehyde-3-phosphate dehydrogenase (GAPDH) serving as the loading control. **d,** Comparison of genes coding for proteins which were perturbed on Fig. 4j in hypotetraploid RPT cell lines and their diploid parental wild type counterparts.



Extended Data Figure 6. Acute spindle compression increases metaphase plate width and thickness without affecting spindle length and blocking cell proliferation. **a**, Phase diagram of the metaphase plate width, dimension perpendicular to the direction of external force, W_z , and **b**, the metaphase plate height, dimension in the direction of external force, W_y , as a function of Young's modulus and sphere radius for compression coefficient $k = 100$ pN/ μm . **c**, Metaphase plate width in U2OS control (left) and RPE1 control (right) cells for three time points related to cell compression. **d**, Metaphase plate thickness for three time points related to compression of U2OS control (left) and RPE1 control (right) cells. **e**, Spindle length for three time points related to compression of U2OS control (left), U2OS cells in mitosis with unreplicated genome (MUG) (middle) and RPE1 control (right) cells. **f**, Spindle height (magenta) and spindle width (green) for three time points related to compression of control RPE1 cells. **g**, Time-lapse of control RPE1 cells stably expressing CENP-A-GFP and centrin-GFP (centrioles, encircled) (color-coded for depth) in compression experiment, with SiR-tubulin (MTs, grey) and Hoechst 33342 labelled DNA (cyan). **h**, Angle (in degrees) between pole and outermost kinetochore fiber for three time points related to compression of U2OS cells in MUG (left) and control RPE1 cells (right). **i**, Changes (Δ) in height (left) and width (middle) during compression and metaphase duration histogram after compression for control RPE1 cells that either divided (light grey) or did not divide (dark grey) during imaging (right). Colored points on left and middle represent individual cells; the black line shows the mean, with light and dark

grey areas marking 95% confidence intervals for the mean and standard deviation. p-values (Student's t-test) are shown above. **j**, Mean \pm SEM for spindle width versus spindle length for compression experiments; lines connect corresponding mean values before and after compression. Number of cells: 12, 11, 21. **k**, Phase diagram of metaphase plate width W_z , as a function of chromosome radius and spindle length for $k = 100$ pN/ μ m. In (c), (d), (e), (f) and (h) black line, mean value; shaded area, 95% confidence interval. Number of cells - (c) 12 (left); 21 (right); (d) 12 (left); 21 (right); (e) 12 (left), 21 (middle), 11 (right); (f) 21; (h) 21 (left), 11 (right); (i) 14, 6 (left); 14, 6 (middle); 20 (right); (j) 12 (left), 21 (middle), 11 (right). In (a), (b), and (k) parameters are as in (Fig. 3), unless stated otherwise. Abbreviations: Exp., experiment. Number of cells equals the number of independent experiments.



Extended Data Figure 7. Scheme of the model. **a**, Three-dimensional scheme of the metaphase spindle with 19 chromosomes for the parameter values from Fig. 3. Two cross-sections of the spindle which contain the left spindle pole, and the metaphase plate are numbered (1) and (2) respectively, whereas a single bundle is numbered (3). Chromosomes are shown in light gray, microtubule bundles in gray, and spindle poles in dark gray. Two individual bundles, labeled i and j , are shown by solid and dashed green lines, respectively. Coordinates of the right and left spindle poles are shown by triples of numbers. **b**, Scheme of the left spindle pole in side view (left) and end-on view (right). The forces exerted by the pole on the microtubule bundle, $F_{i,left}$ and $F_{j,left}$, are shown in orange for bundles i and j , respectively. The positions of the left microtubule bundle ends are shown as green dots for the bundles i and j , and as black dots for the other bundles. The radius vectors for the left microtubule ends, $d_{i,left}$ and $d_{j,left}$, are shown in black. The coordinate of the left spindle pole is shown by a triple of numbers. The lattice parameter, a_0 , is shown in the end-on view. **c**, Scheme of the metaphase plate in end-on view. The repulsive forces F_{ij} and F_{ji} mutually exerted between the bundles i and j , respectively, are shown in orange. The reduction of distance, h_{ij} , between the chromosomes corresponding to bundles i and j is shown in black. The coordinate of the metaphase plate center is shown by a triple of numbers. **d**, Scheme of the microtubule bundle i . The forces exerted by the pole on the left and right ends of microtubule bundles, $F_{i,left}$ and $F_{i,right}$ respectively, as well as the repulsive force exerted by the neighboring chromosomes, $F_{i,chr}$, are shown in orange. The radius vector at the coordinate x , $r_i(x)$, the

tangent, $t_i(x)$, the radius vector of the chromosome, $r_{i,\text{chr}}(x)$, and the radius of the chromosome, R , are shown in black. The coordinates of the left and right poles, as well as the center of the metaphase plate, are shown by triples of numbers. The contour length for bundle i is shown in the inset. The coordinate systems of the entire spindle and its individual components are shown in insets within each panel.

Extended Data Table 1. Measurements of metaphase plate width, spindle length, and spindle width from published images of mitotic spindles in eukaryotes with diverse ploidy levels, genome sizes, and chromosome numbers.

Species and mitosis type	Cell type and ploidy	Genome size (Mbp)	Chromosome number	Spindle length (µm)	Spindle width (µm)	Plate width (µm)	References for genome size and chromosome number	References for spindle length and width	References for metaphase plate width
<i>Shizosaccharomyces pombe</i>	Haploid	14	3	2.3	0.38	2.9	NCBI GenBank	(106)	(107) ^a
<i>Saccharomyces cerevisiae</i>	Diploid	24	32	1.5	0.35	2.3	NCBI GenBank	(108)	(109) ^a
<i>Corallochytrium limacisporum</i>	Unknown, assumed diploid	24.1	Unknown	1.9	1.0	1.8	(110)	(111, Extended data Fig. 9C) ^b	(111, Extended data Fig. 9C) ^b
<i>Capsasphora owczarzaki</i>	Unknown, assumed diploid	27.9	Unknown	1.5	Unknown	1.6	(110)	(112, Fig. 2B) ^b	(112, Fig. 2B) ^{b, c}
<i>Dictyostelium discoideum</i>	Haploid	34	6	2.1	0.6	3.0	(113)	(114)	(115) ^a
<i>Chromosphaera perkinsii</i>	Unknown, assumed diploid	34.6	Unknown	3.91	2.28	2.5	(110)	(111)	(111)
<i>Creolimax fragrantissima</i>	Unknown, assumed diploid	42.9	Unknown	2.4	1.2	Unknown	(110)	(111, Fig. 4A) ^b	Not found
<i>Naegleria gruberi</i>	Diploid	82	12	7.4	3.7	4.2	(113)	(116)	(116, Fig. 4) ^b
<i>Chlamydomonas reinhardtii</i>	Haploid	120	17	3.70	1.80	3.4	NCBI GenBank	(117)	(118, Fig. 7) ^{b, c}
<i>Sphaerofarma arctica</i>	Unknown, assumed diploid	120.9	Unknown	3.45	1.6	4.7	(110)	(111, Fig. 2C, Fig. 2D) ^b	(111) ^a
<i>Caenorhabditis elegans</i>	Embryo, 200-cell stage, diploid	200	41	3.0	3.0	3.3	NCBI GenBank	(18)	(18)
<i>Drosophila melanogaster</i>	S2 cells, diploid	260	8	11.2	6.9	8.0	NCBI GenBank	(59, Fig. 2B) ^b	(59, Fig. 1C) ^b
<i>Arabidopsis thaliana</i>	Root tips cell, diploid	270	10	7.8	4.6	6.9	NCBI GenBank	(119, Fig. 3) ^b	(120)
<i>Galus gallus</i>	DT40 B lymphocyte, diploid	2400	78	10.1	8.4	10.8	NCBI GenBank	(121, Fig. 2a) ^b	(121, Fig. 2a) ^b
<i>Xenopus tropicalis</i>	Embryo, stage 36, diploid	3400	20	9.8	7.3	11.3	(20)	(20, Fig. S4E, Fig. 4C) ^b	(20, Fig. S4E) ^b
<i>Zea mays</i>	Root tip cell, diploid	4730	20	7.6 ^e	7.6	10.7	NCBI GenBank	(122)	(122)
<i>Mus musculus</i>	mESC, diploid	5380	40	11.9	8.3	12.1	(19)	(19)	(19)
<i>Xenopus laevis</i>	Embryo, stage 36, allotetraploid	6000 ^d	36	15.3	9.8	14.8	(20)	(20, Fig. 4C) ^b	(20, Fig. S4E) ^b
<i>Potorous tridactylus</i>	Ptk1, diploid	6025	12	15.21	7.45	15.95	Animal genome size database	(123, Fig 1a) ^b	(124, Fig. 2E) ^b
<i>Muntiacus muntjak</i>	Fibroblast, diploid	6494	6	10.82	5.82	15.65	(125)	(126, Fig. S2A, Fig. S2A') ^b	(127, Fig. 3A), (126, Fig. 1A) ^b
<i>Homo sapiens</i>	HEK293, hypotriploid	8000	64, modal	11.8	10.4	14.2	(19)	(19)	(19)
<i>Homo sapiens</i>	HeLa, hypertriploid	9720	82, modal	13.7	11.2	15.1	(19)	(19)	(19)
<i>Hordeum vulgare</i>	Root tip cell, diploid	10200	14	13.6 ^e	11.2	15.9	NCBI GenBank	(122)	(122)
<i>Xenopus longipes</i>	Embryo, stage 36, dodecaploid	15000 ^d	108	16.3	10.5	17.5	(20)	(20, Fig. 4C) ^b	(20, Fig. S4E) ^b
<i>Triticum aestivum</i>	Root tip cell, allohexaploid	34000	42	18.6 ^e	23.1	27.2	NCBI GenBank	(122)	(122)
<i>Taricha granulosa</i>	Lung cell, diploid	70959	22	44.98	19.57	40.35	Animal genome size database	(128, Fig. 1, 2), (129, Fig. 1B), (130, Fig. 2) ^b	(128, Fig. 1, 2), (129, Fig. 1B), (130, Fig. 2) ^b

Values for spindle and genome parameters across different species with references. Superscripts: a, DNA fills the nucleus; b, measured or estimated from given figures; c, spindle has a discernible metaphase plate; d, genome size normalized to *X. tropicalis*, e, spindle with unfocused poles.

Extended Data Table 2. Measurements of metaphase plate width and spindle length from published images of acentriolar mitotic and meiotic spindles across different species and ploidy levels.

Species and system	Ploidy and stage	Metaphase plate width (μm)	Spindle length (μm)	References
Human HAP1 cells	Near-haploid	9.65	7.98	(41)
	Diploid	11.42	8.20	(41)
Human oocytes	Metaphase I	15.53 \pm 1.83	13.7 \pm 1.05	(43, 45, 46, 48)
	Metaphase II	11.55 \pm 1.10	12.77 \pm 1.08	(43, 45, 46, 48)
Mouse oocytes	Metaphase I	14.96 \pm 3.11	18.95 \pm 2.97	(44, 47)
	Metaphase II	9.97 \pm 1.68	17.87 \pm 1.74	(44, 47)
Mouse acentriolar blastocysts	Diploid ¹	17.52 \pm 0.51	19.23 \pm 0.80	(50)
	Tetraploid ¹	20.47 \pm 0.55	18.43 \pm 1.77	(50)
Porcine oocytes	Diploid metaphase II	6.49	6.40	(49)
	Tetraploid metaphase II	8.19	7.03	(49)

Data are presented as a single value, when only one data point was available, or mean \pm SEM, when more data points were analyzed. Superscripts: 1, includes data from 8-cell control and 4-cell tetraploid embryos, as well as 16-cell control and 8-cell tetraploid embryos. Tetraploid mouse acentriolar blastocysts contained both binuclear and mononuclear cells. See references for detailed protocols.

Extended Data movie legends

Extended Data Movie 1. Diploid RPE1 cells and its derivatives of different ploidies during interphase and mitosis. The combined movie shows live-cell imaging of the following: a diploid RPE-1 cell expressing H2B-GFP (modal chromosome number = 46); a hypotetraploid RPT1 cell expressing H2B-GFP (modal chromosome number = 80); a newly generated mononuclear tetraploid cell with p53 knockdown expressing H2B-Dendra2 (modal chromosome number = 92); and a newly generated mononuclear hypooctaploid cell expressing H2B-GFP (modal chromosome number = 160). Tetraploid and hypooctaploid cells were generated using the procedure detailed in Extended Data Figure 2c and the Methods section. The movie plays at 7 frames per second. To ensure consistency, the first, second, and fourth segments include duplicate final frames of metaphase to match the number of frames in the third segment.

Extended Data Movie 2. Acute compression of untreated spindles and spindles with unreplicated genomes in U2OS cells. The combined movie shows live-cell imaging of z-stacks from hypertriploid U2OS cells expressing CENP-A-GFP (magenta), α -tubulin-mCherry (gray), and stained with Hoechst-DNA (cyan) under the following conditions: untreated control before compression (top left), mitosis with unreplicated genome (MUG) before compression (bottom left), untreated control during compression (top middle), MUG during compression (bottom middle), untreated control after compression (top right), and MUG after compression (bottom right). MUG cells were generated using the procedure detailed in the Methods section. All z-stacks include the same number of slices, with the 0 point defined at the center of the mitotic spindle. The movie plays at 7 frames per second.

Extended Data references

106. Ding, R., McDonald, K. L. & McIntosh, J. R. Three-dimensional reconstruction and analysis of mitotic spindles from the yeast, *Schizosaccharomyces pombe*. *J. Cell Biol.* **120**, 141–151 (1993).
107. Zareiesfandabadi, P. & Elting, M. W. Force by minus-end motors Dhc1 and Klp2 collapses the *S. pombe* spindle after laser ablation. *Biophys. J.* **121**, 263–276 (2022).
108. Winey, M. *et al.* Three-dimensional ultrastructural analysis of the *Saccharomyces cerevisiae* mitotic spindle. *J. Cell Biol.* **129**, 1601–1615 (1995).
109. Verdaasdonk, J. S., Gardner, R., Stephens, A. D., Yeh, E. & Bloom, K. Tension-dependent nucleosome remodeling at the pericentromere in yeast. *Mol. Biol. Cell* **23**, 2560–2570 (2012).
110. Grau-Bové, X. *et al.* Dynamics of genomic innovation in the unicellular ancestry of animals. *eLife* **6**, e26036 (2017).
111. Shah, H. *et al.* Life-cycle-coupled evolution of mitosis in close relatives of animals. *Nature* **630**, 116–122 (2024).
112. Pérez-Posada, A., Dudin, O., Ocaña-Pallarès, E., Ruiz-Trillo, I. & Ondracka, A. Cell cycle transcriptomics of *Capsaspora* provides insights into the evolution of cyclin-CDK machinery. *PLoS Genet.* **16**, e1008584 (2020).
113. Fritz-Laylin, L. K. *et al.* The genome of *Naegleria gruberi* illuminates early eukaryotic versatility. *Cell* **140**, 631–42 (2010).
114. Moens, P. B. Spindle and kinetochore morphology of *Dictyostelium discoideum*. *J. Cell Biol.* **68**, 113–122 (1976).
115. Catalano, A. & O’Day, D. H. Rad53 homologue forkhead-associated kinase A (FhkA) and Ca²⁺-binding protein 4a (CBP4a) are nucleolar proteins that differentially redistribute during mitosis in *Dictyostelium*. *Cell Div.* **8**, 4 (2013).
116. Velle, K. B. *et al.* *Naegleria*’s mitotic spindles are built from unique tubulins and highlight core spindle features. *Curr Biol* **32**, 1247-1261 e6 (2022).
117. O’Toole, E., Morphew, M. & McIntosh, J. R. Electron tomography reveals aspects of spindle structure important for mechanical stability at metaphase. *Mol. Biol. Cell* **31**, 184–195 (2020).
118. Esparza, J. M. *et al.* Katanin localization requires triplet microtubules in *Chlamydomonas reinhardtii*. *PLoS One* **8**, e53940 (2013).
119. Ambrose, J. C. & Cyr, R. The Kinesin ATK5 Functions in Early Spindle Assembly in *Arabidopsis*. *Plant Cell* **19**, 226–236 (2007).
120. Romeiro Motta, M. *et al.* B1-type cyclins control microtubule organization during cell division in *Arabidopsis*. *EMBO Rep.* **23**, e53995 (2022).
121. Ribeiro, S. A. *et al.* Condensin Regulates the Stiffness of Vertebrate Centromeres. *Mol. Biol. Cell* **20**, 2371–2380 (2009).
122. Zhang, H. & Dawe, R. K. Total centromere size and genome size are strongly correlated in ten grass species. *Chromosome Res.* **20**, 403–412 (2012).
123. Wan, X., Cimini, D., Cameron, L. A. & Salmon, E. D. The coupling between sister kinetochore directional instability and oscillations in centromere stretch in metaphase PtK1 cells. *Mol. Biol. Cell* **23**, 1035–1046 (2012).

124. O'Connell, C. B. & Khodjakov, A. L. Cooperative mechanisms of mitotic spindle formation. *J. Cell Sci.* **120**, 1717–1722 (2007).
125. Plačková, K., Bureš, P. & Zedek, F. Centromere size scales with genome size across Eukaryotes. *Sci. Rep.* **11**, 19811 (2021).
- 126 Almeida, A. C. *et al.* Augmin-dependent microtubule self-organization drives kinetochore fiber maturation in mammals. *Cell Rep.* **39**, 110610 (2022).
127. Drpic, D. *et al.* Chromosome Segregation Is Biased by Kinetochore Size. *Curr. Biol.* **28**, 1344-1356.e5 (2018).
128. Mitchison, T. J. & Salmon, E. D. Poleward kinetochore fiber movement occurs during both metaphase and anaphase-A in newt lung cell mitosis. *J. Cell Biol.* **119**, 569–582 (1992).
129. Waters, J. C., Skibbens, R. V. & Salmon, E. D. Oscillating mitotic newt lung cell kinetochores are, on average, under tension and rarely push. *J. Cell Sci.* **109**, 2823–2831 (1996).
130. Rieder, C. L. & Khodjakov, A. Mitosis Through the Microscope: Advances in Seeing Inside Live Dividing Cells. *Science* **300**, 91–96 (2003).